

# Larger sizes of massive quiescent early-type galaxies in clusters than in the field at $0.8 < z < 1.5$

L. Delaye,<sup>1,2\*</sup> M. Huertas-Company,<sup>1,3</sup> S. Mei,<sup>1,3</sup> C. Lidman,<sup>4</sup> R. Licitra,<sup>1</sup>  
A. Newman,<sup>5</sup> A. Raichoor,<sup>1</sup> F. Shankar,<sup>1</sup> F. Barrientos,<sup>6</sup> M. Bernardi,<sup>7</sup> P. Cerulo,<sup>8</sup>  
W. Couch,<sup>8</sup> R. Demarco,<sup>9</sup> R. Muñoz,<sup>6</sup> R. Sánchez-Janssen<sup>10</sup> and M. Tanaka<sup>11</sup>

<sup>1</sup>GEPI, Paris Observatory, 77 av. Denfert Rochereau, F-75014 Paris, France

<sup>2</sup>CEA-Saclay, DSM/IRFU/Sap, F-91191 Gif-sur-Yvette, France

<sup>3</sup>University Denis Diderot, 4 Rue Thomas Mann, F-75205 Paris, France

<sup>4</sup>Australian Astronomical Observatory, PO Box 296 Epping, NSW 1710, Australia

<sup>5</sup>Cahill Center for Astronomy and Astrophysics, California Institute of Technology, MS 249-17, Pasadena, CA 91125, USA

<sup>6</sup>Instituto de Astrofísica, Facultad de Física, Pontificia Universidad Católica de Chile, Av. Vicuña Mackenna 4860, 7820436 Macul, Santiago, Chile

<sup>7</sup>Department of Physics and Astronomy, University of Pennsylvania, 209 South 33rd Street, Philadelphia, PA 19104, USA

<sup>8</sup>Centre for Astrophysics & Supercomputing, Swinburne University of Technology, PO Box 218, Hawthorn, VIC 3122, Australia

<sup>9</sup>Department of Astronomy, Universidad de Concepción, Casilla 160-C, Concepción, Chile

<sup>10</sup>European Southern Observatory, Alonso de Crdova 3107 Vitacura, Santiago, Chile

<sup>11</sup>Institute for the Physics and Mathematics of the Universe, The University of Tokyo, 5-1-5 Kashiwanoha, Kashiwa-shi, Chiba 277-8583, Japan

Accepted 2014 March 9. Received 2014 February 28; in original form 2013 May 2

## ABSTRACT

We analyse the mass–size relation of  $\sim 400$  quiescent massive ETGs ( $M_*/M_\odot > 3 \times 10^{10}$ ) hosted by massive clusters ( $M_{200} \sim 2\text{--}7 \times 10^{14} M_\odot$ ) at  $0.8 < z < 1.5$ , compared to those found in the field at the same epoch. Size is parametrized using the mass-normalized *B*-band rest-frame size,  $\gamma = R_e/M_{11}^{0.57}$ . We find that the  $\gamma$  distributions in both environments peak at the same position, but the distributions in clusters are more skewed towards larger sizes. This tail induces average sizes  $\sim 30\text{--}40$  per cent larger for cluster galaxies than for field galaxies of similar stellar mass, while the median sizes are statistically the same with a difference of  $\sim 10 \pm 10$  per cent. Since this size difference is not observed in the local Universe, the evolution of average galaxy size at fixed stellar mass from  $z \sim 1.5$  for cluster galaxies is less steep at more than  $3\sigma$  ( $\propto(1+z)^{-0.53 \pm 0.04}$ ) than the evolution of field galaxies ( $\propto(1+z)^{-0.92 \pm 0.04}$ ). The difference in evolution is not measured when the median values of  $\gamma$  are considered:  $\propto(1+z)^{-0.84 \pm 0.04}$  in the field versus  $\propto(1+z)^{-0.71 \pm 0.05}$  in clusters. In our sample, the tail of large galaxies is dominated by galaxies with  $3 \times 10^{10} < M_*/M_\odot < 10^{11}$ . At this low-mass end, the difference in the average size is better explained by the accretion of new galaxies that are quenched more efficiently in clusters and/or by different morphological mixing in the cluster and field environments. If part of the size evolution would be due to mergers, the difference that we see between cluster and field galaxies could be caused by higher merger rates in clusters at higher redshift, when galaxy velocities are lower.

**Key words:** galaxies: clusters: general–galaxies: elliptical and lenticular–galaxies: evolution.

## 1 INTRODUCTION

The mass assembly of the most massive galaxies in the universe is still an open issue. For a long time, the uniformity of their stellar populations together with their regular morphology have been interpreted as signs of a relatively quiet life, dominated by a

strong starburst at very early epochs followed by a passive evolution (Partridge & Peebles 1967; Larson 1975). The discovery of a population of massive early-type galaxies (ETGs) at high redshift, on average 2–5 times more compact than their local counterparts indicates a more active life (Daddi et al. 2005; Trujillo et al. 2006). Even though the exact abundance of these compact objects in the local universe is still debated today (Valentinuzzi et al. 2010a; Trujillo, Carrasco & Ferré-Mateu 2012; Poggianti et al. 2013), it is accepted that at least a fraction of massive ETGs needs to

\*E-mail: marc.huertas@obspm.fr

significantly increase the size over the last 10 Gyr (Buitrago et al. 2008; van Dokkum et al. 2008; Martinez-Manso et al. 2011; Saracco, Longhetti & Gargiulo 2011; van de Sande et al. 2011; Newman et al. 2012; Raichoor et al. 2012, and references therein).

Two physical processes are usually invoked to explain such a growth but none of them is able to reproduce all the observed trends. Intense AGN activity can expel the gas of the galaxy in a relatively short amount of time leading to a redistribution of the gravitational potential and hence to an increase of the size (Fan et al. 2008, 2010). Recent numerical simulations by Ragone-Figueroa & Granato (2011) have shown however that the typical time-scale for this process is only of a few Myr which seems difficult to reconcile with the low dispersion in the ages and sizes of compact galaxies at high redshift (e.g. Trujillo et al. 2011).

On cosmological time-scales, dry minor mergers can also lead to a growth of the galaxy by spreading stars in the outer parts after the merger event, without significantly increasing the stellar mass (Bernardi 2009; Bezanson et al. 2009; Hopkins et al. 2009; Naab, Johansson & Ostriker 2009; Shankar et al. 2010; Shankar et al., in preparation; van Dokkum et al. 2010). While major mergers also contribute (e.g. Bluck et al. 2009; López-Sanjuan et al. 2010), they cannot be the main driver as the number of mergers required leads to inconsistencies with the observed mass function (e.g. López-Sanjuan et al. 2009). However, minor mergers are particularly attractive because they can explain many of the observed properties of massive objects (scatter, inside-out growth, etc.) and they are known to be frequent events in a cold dark matter cosmology. Extremely deep imaging of nearby ETGs has indeed revealed signs of disturbances in the outskirts of many of these galaxies (Duc et al. 2011). The direct observation of such minor mergers remains a challenge at high redshift, and there are still several open questions (e.g. Díaz-García et al. 2013). Newman et al. (2012) found that the number of observed satellites around massive galaxies can account for the measured size growth from  $z = 1$  only if short dynamical time-scales are assumed. Similar conclusions are also reached by López-Sanjuan et al. (2012) who invoked a progenitor bias to explain the excess of growth they measure. Huertas-Company et al. (2013b) also showed that several hierarchical models based on the Millennium merger trees struggle to fully reproduce the amount of evolution reported by the data at fixed stellar mass.

Environment is an additional variable that can be analysed to disentangle between different scenarios, as we have shown in several recent works (Raichoor et al. 2012; Huertas-Company et al. 2013b; Shankar et al. 2013). Several hierarchical models predict a correlation between galaxy size and the environment in which the galaxy lives, with larger galaxies in denser environments (Shankar et al., in preparation). Observational results up to now have been controversial though. In the local universe, Huertas-Company et al. (2013b) did not find any trend with environment (see also Guo et al. 2010; Weinmann et al. 2009) for massive galaxies in the SDSS. A similar result was already pointed out by Maltby et al. (2010) who did not find any significant structural difference between ETGs living in clusters and in the field at  $z < 0.4$  (see also Gutierrez et al. 2004). More recently Fernandez-Lorenzo (2013) has compared the mass-size relation (MSR) of isolated and non-isolated ETGs and did not find any difference either. Cappellari (2013) has also addressed this issue using kinematic data and also found no significant difference between the MSRs of Coma and field ETGs. All these results seem to reveal a universal MSR independent of environment at  $z \sim 0$ . Poggianti et al. (2013) reported however that cluster galaxies are slightly smaller ( $1\sigma$ ) than field galaxies at fixed stellar mass (see

also Valentiniuzzi et al. 2010a). At  $z < 1$ , Huertas-Company et al. (2013b) again did not find any difference between group and field galaxies, whereas Cooper et al. (2012) found that galaxies living in denser environments are larger. However, they measured the density of the environment in a different way. At higher redshifts ( $z > 1$ ), the situation is less clear since having a statistically significant sample of massive clusters at  $z > 1$  was almost impossible until very recently. The first works exploring that redshift range were based on one single cluster (Raichoor et al. 2012; Papovich et al. 2012) and results are not in agreement (e.g. Bassett et al. 2013; Newman et al. 2013).

In this work, we make a step forward by analysing a sample of nine well-known massive clusters ( $M_h \sim 2-7 \times 10^{14} M_\odot$ ) at  $0.8 \lesssim z \lesssim 1.5$  from the HAWK-I Cluster survey (Lidman et al. 2013), to look for differences in the sizes of massive ETGs in cluster and field environments. All clusters but two have extended X-ray emission, between 20 and 100 spectroscopically confirmed members and have been observed with at least two filters with the *Hubble Space Telescope* (*HST*) Advanced Camera for Surveys (ACS).

The paper is organized as follows: in Section 2, we present the data set and describe the general methodology used to estimate sizes, masses and morphologies of cluster galaxies. In Section 3, we describe the field galaxy sample used for comparison. We show our results in Section 4 and discuss them in Section 5.

Throughout the paper, magnitudes are given in the AB system (Oke & Gunn 1983; Sirianni et al. 2005) for all passbands. We assume a standard cosmological model with  $\Omega_M = 0.3$ ,  $\Omega_\Lambda = 0.7$  and  $H_0 = 70 \text{ km s}^{-1} \text{ Mpc}^{-1}$  and use a Chabrier initial mass function (IMF).

## 2 DATA AND SAMPLE SELECTION

### 2.1 Cluster selection

Our targets have been selected according to the following criteria: (1) they cover a broad redshift range  $0.84 < z < 1.45$ ; (2) they have been imaged with the *HST*/ACS in at least two bandpasses and have deep ground-based images in the near-IR; (3) they have at least 10 spectroscopically confirmed cluster members.

All clusters have *HST*/ACS WFC (Wide Field Camera) images in at least two bandpasses. The ACS WFC resolution is  $0.05 \text{ arcsec pixel}^{-1}$ , and its field of view is  $210 \text{ arcsec} \times 204 \text{ arcsec}$ . The ACS/WFC PSF width is around  $0.11 \text{ arcsec}$ . Our ACS/WFC images were mostly obtained in a programme designed to find Type Ia supernovae in distant galaxy clusters (Dawson et al. 2009). See Meyers et al. (2012) for a description of how these data were processed. Three clusters (see below): RDCS J1252–2927, XMMU J2235.3–2557 and RX J0152–1357 had been previously targeted with the ACS camera on *HST* in the context of the ACS Intermediate Redshift Cluster Survey (Ford 2004; Postman et al. 2005; Mei et al. 2009) and these data have been included.

Eight of the nine clusters in this paper were targeted in the European Southern Observatory (ESO) HAWK-I<sup>1</sup> Cluster survey (HCS; Lidman et al. 2013). The HCS is a near-IR imaging survey that targeted nine well-known high-redshift galaxy clusters between  $z = 0.8$  and  $1.5$ . The aim of the survey was to obtain deep, high-resolution images of a sample of clusters for the purpose of studying

<sup>1</sup> High Acuity Wide-field K-band Imager

**Table 1.** HCS data. For each cluster, we indicate the available filters together with the exposure time in seconds. <sup>1</sup>From HAWK-I, <sup>2</sup>from ISAAC, <sup>3</sup>from SOFI. <sup>a</sup>Demarco et al. (2005, 2010), <sup>b</sup>Gilbank et al. (2008, 2011); Meyers et al. (2010), <sup>c</sup>Santos et al. (2009), <sup>d</sup>Meyers et al. (2010); Gilbank et al. (2011), <sup>e</sup>Bremer et al. (2006); Meyers et al. (2010), <sup>f</sup>Demarco et al. (2007), <sup>g</sup>Rosati et al. (2009), <sup>h</sup>Hilton et al. (2010).

Cluster	Filters	$N_{z\text{spec}}$
RX J0152–1357	$r_{625}$ (19 000), $i_{775}$ (19 200), $z_{850}$ (19 000), $K_s^1$ (9600)	107 <sup>a</sup>
RCS 2319+0038	$i_{775}$ (2400), $z_{850}$ (6800), $K_s^1$ (9600), $J^2$ (2970)	28 <sup>b</sup>
XMM J1229+0151	$i_{775}$ (4110), $z_{850}$ (10 940), $K_s^1$ (11 310), $J^3$ (2280)	26 <sup>c</sup>
RCS 0220–0333	$i_{775}$ (2955), $z_{850}$ (14 420), $K_s^1$ (9600), $J^2$ (3330)	11 <sup>d</sup>
RCS 2345–3633	$i_{775}$ (4450), $z_{850}$ (9680), $K_s^1$ (9600), $J^2$ (2520)	23 <sup>d</sup>
XMM J0223–0436	$i_{775}$ (3380), $z_{850}$ (14 020), $K_s^1$ (9600), $J^1$ (11 040)	27 <sup>e</sup>
RDCS J1252–2927	$i_{775}$ (29 945), $z_{850}$ (57 070), $K_s^2$ (81 990), $J^2$ (86 640)	31 <sup>f</sup>
XMMU 2235–2557	$i_{775}$ (8150), $z_{850}$ (14 400), $K_s^1$ (10 560), $J^1$ (10 740)	34 <sup>g</sup>
XMM J2215–1738	$i_{775}$ (3320), $z_{850}$ (16 935), $K_s^1$ (9600), $J^1$ (14 400)	48 <sup>h</sup>

**Table 2.** Cluster physical properties from Jee et al. (2011). From left to right, columns show the cluster redshift, the velocity dispersion, the X-ray temperature, the X-ray mass, the virial radius and the lensing mass. <sup>a</sup>Demarco et al. (2005), <sup>b</sup>Faloon et al. (2013), <sup>c</sup>Santos et al. (2009), <sup>d</sup>Jee et al. (2011), <sup>e</sup>Meyers et al. (2012), <sup>f</sup>Demarco et al. (2007), <sup>g</sup>Rosati et al. (2009), <sup>h</sup>Hilton et al. (2010), <sup>1</sup>Ettori et al. (2009), <sup>2</sup>Hicks et al. (2008), <sup>3</sup>Santos et al. (2009), <sup>4</sup>Bremer et al. (2006), <sup>5</sup>Ettori et al. (2009), <sup>6</sup>Rosati et al. (2009), <sup>7</sup>Hilton et al. (2010).

Cluster	$z_{cl}$	$\sigma_{vel}$ (km s <sup>-1</sup> )	$T$ (keV)	$M_{200}^X$ (10 <sup>14</sup> M <sub>⊙</sub> )	$R_{200}$ (Mpc)	$M_{200}^L$ (10 <sup>14</sup> M <sub>⊙</sub> )
RX J0152–1357	0.84	919 ± 168 <sup>a</sup>	6.7 ± 1.0 <sup>1</sup>	7.3 <sup>+1.8</sup> <sub>-1.7</sub>	1.17 <sup>+0.09</sup> <sub>-0.06</sub>	4.4 <sup>+0.7</sup> <sub>-0.5</sub>
RCS2 319+0038	0.90	1202 ± 233 <sup>b</sup>	6.2 <sup>+0.92</sup> <sub>-0.8</sub>	5.4 <sup>+1.2</sup> <sub>-1.0</sub>	1.22 <sup>+0.15</sup> <sub>-0.13</sub>	5.8 <sup>+2.3</sup> <sub>-1.6</sub>
XMM J1229+0151	0.98	683 ± 62 <sup>c</sup>	6.4 <sup>+0.73</sup> <sub>-0.6</sub>	5.7 <sup>+1.0</sup> <sub>-0.8</sub>	1.12 <sup>+0.11</sup> <sub>-0.10</sub>	5.3 <sup>+1.7</sup> <sub>-1.2</sub>
RCS 0220–0333	1.03	–	–	–	1.09 <sup>+0.12</sup> <sub>-0.11</sub>	4.8 <sup>+1.8</sup> <sub>-1.3</sub>
RCS 2345–3633	1.04	670 ± 190 <sup>d</sup>	–	–	0.87 <sup>+0.11</sup> <sub>-0.10</sub>	2.4 <sup>+1.1</sup> <sub>-0.7</sub>
XMM J0223–0436	1.22	799 ± 129 <sup>e</sup>	3.8 <sup>-1.9</sup> <sub>-1.9</sub> <sup>4</sup>	2.4 <sup>-1.5</sup> <sub>-1.5</sub>	1.18 <sup>+0.12</sup> <sub>-0.11</sub>	7.4 <sup>+2.5</sup> <sub>-1.8</sub>
RDCS J1252–2927	1.23	747 <sup>+74f</sup> <sub>-84</sub>	7.6 ± 1.2 <sup>5</sup>	4.4 <sup>+1.1</sup> <sub>-1.0</sub>	1.14 <sup>+0.06</sup> <sub>-0.06</sub>	6.8 <sup>+1.2</sup> <sub>-1.0</sub>
XMMU 2235–2557	1.39	802 <sup>+77g</sup> <sub>-48</sub>	8.6 <sup>+1.36</sup> <sub>-1.2</sub>	6.1 <sup>+1.4</sup> <sub>-1.2</sub>	1.13 <sup>+0.08</sup> <sub>-0.07</sub>	7.3 <sup>+1.7</sup> <sub>-1.4</sub>
XMM J2215–1738	1.45	720 ± 110 <sup>h</sup>	4.1 <sup>+0.67</sup> <sub>-0.9</sub>	2.0 <sup>+0.5</sup> <sub>-0.6</sub>	0.9 <sup>+0.17</sup> <sub>-0.14</sub>	4.3 <sup>+3.0</sup> <sub>-1.7</sub>

the impact of environment on the evolution of cluster members. The ninth cluster in our sample, RDCS J1252–2827, was imaged with ISAAC<sup>2</sup> (Lidman et al. 2004). For some clusters, we also use  $J$ -band images from ESO/SOFI.<sup>3</sup>

A summary of the observations is given in Table 1 and the physical properties of each cluster are summarized in Table 2 (see also Appendix A for more details on each individual cluster). We also show in Figs 1 and 2a colour images of two of the clusters in our sample.

## 2.2 Photometry and object detection

Object detection is performed in the  $K_s$  band using SExtractor (Bertin & Arnouts 1996) and then the resulting catalogue is matched in the other wavelengths, to obtain MAG\_AUTO magnitudes. When using point spread function (PSF) matched magnitudes we obtain similar results on the final stellar mass–sizes. Colours are computed with aperture magnitudes within an effective radius for each galaxy (estimated from the 2D Sérsic best fit – see Section 2.3), to avoid systematics due to internal galaxy gradients (van Dokkum et al. 1998, 2000; Scodreggio 2001).

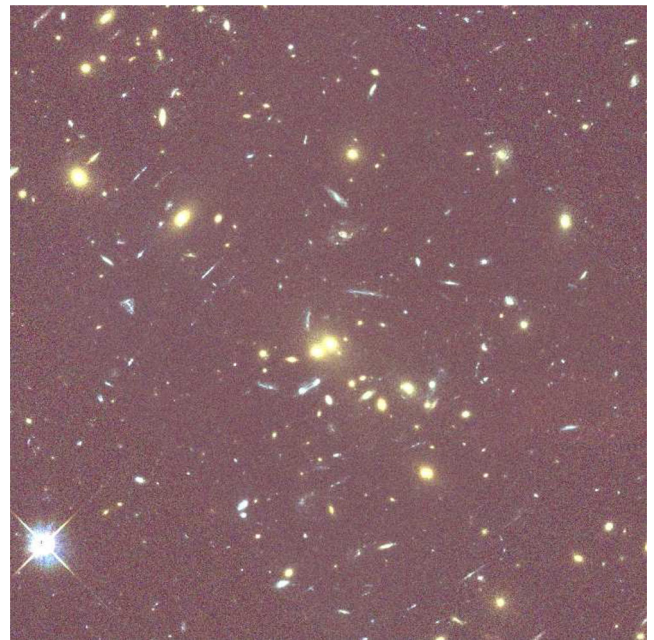


**Figure 1.** Color image of the centre of RX J0152–1357 with  $r_{625}$ ,  $i_{775}$  and  $z_{850}$  bandpasses. The field size is 75 arcsec × 75 arcsec, corresponding to 572 × 572 kpc at  $z = 0.84$ .

<sup>2</sup> Infrared Spectrometer And Array Camera

<sup>3</sup> Son of ISAAC.

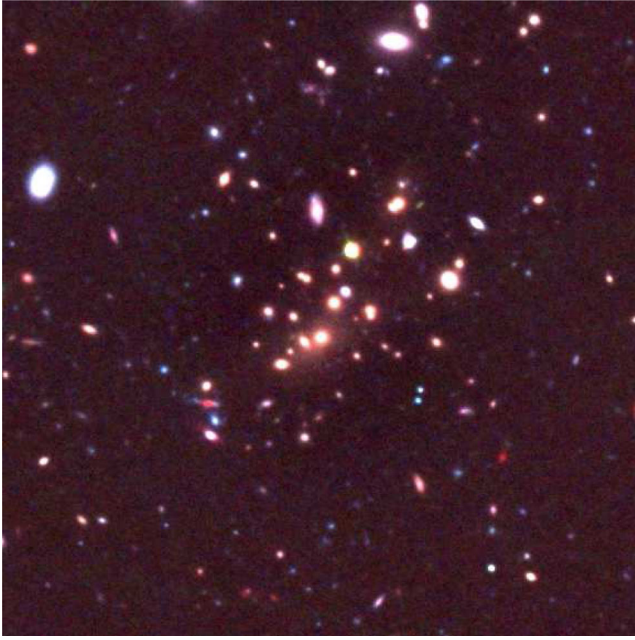


**Figure 2.** Color image of the centre of XMMU J1229+0151 with  $i_{775}$ ,  $z_{850}$  and  $K_s$  bandpasses. The field size is 72 arcsec  $\times$  72 arcsec, corresponding to the same physical size as Fig. 1.

Previous works have shown that photometric errors estimated by SExtractor are underestimated (e.g., Benítez et al. 2004; Giavalisco et al. 2004; Raichoor et al. 2011). We therefore estimate photometric errors on the aperture magnitudes through simulations. For each filter, we simulate 10 000 galaxies between 20 and 25 mag and then drop the simulated objects in a similar background to the one of the real image (see Section 2.3 for more details on the simulations). Simulated galaxies are then recovered with SExtractor. We compare input and output magnitudes, and we estimate the photometric errors as the scatter in magnitude bin of 0.2 mag. For the ACS filters, typical errors on colours within the effective radius are around  $\sim 0.03$ – $0.07$  mag whereas SExtractor errors are in average  $\sim 0.02$  mag. All errors are summarized in Fig. 3. As already shown in previous work (e.g., Benítez et al. 2004; Giavalisco et al. 2004; Mei et al. 2009), we also found a systematic shift of 0.2 mag between input and recovered SExtractor MAG\_AUTO magnitudes.

### 2.3 Sizes

We use GALAPAGOS (Barden et al. 2005) to estimate the sizes of all detected galaxies in the ACS/HST  $i_{775}$  band for the two closest clusters RX0152 at  $z = 0.84$  and RCS2319 at  $z = 0.91$  and the  $z_{850}$  band for the others. Our sizes are therefore derived in the  $B$ -rest-frame band for all clusters. We notice that we do not expect significant differences ( $\sim 20$  per cent) with sizes estimated in redder bands as demonstrated by Cassata et al. (2011), Damjanov et al. (2011), Newman et al. (2010) and Szomoru et al. (2013). In order to check this assumption, we show in Fig. 4a comparison of the sizes obtained for the same objects observed in the  $z$  band (ACS) and in the  $H$  band (WFC3) at  $z \sim 1$  (XMM1229 for which both images are available). As quoted in the mentioned works, there is a systematic difference of 20 per cent with sizes in the  $z$  band being larger with a scatter of 20 per cent.

GALAPAGOS is an IDL-based pipeline to run SExtractor and GALFIT (v3.0.2; Peng et al. 2002) specially designed to be used on large data sets. On each detected source, GALFIT models a galaxy light profile using a 2D Sérsic profile (Sérsic 1968) with a fixed sky value previously estimated by GALAPAGOS. We let the default constraints on the Sérsic index  $n$ , the effective radius  $r_e$ , the axis ratio  $q$ , the position angle PA and the magnitude to run GALFIT:  $0.2 < n < 8$ ,  $0.3 < r_e < 750$  pixel,  $0.0001 < b/a < 1$ ,  $-180^\circ < PA < 180^\circ$ ,  $0 < \text{mag} < 40$  and  $-5 < \delta \text{ mag} < 5$  and use a synthetic PSF from TINYTIM (Krist, Hook & Stoehr 2011).

The sky is fixed and measured by GALAPAGOS before running GALFIT in a three times enlarged isophotal stamp. GALAPAGOS uses a flux growth method to estimate the sky around an object. It calculates the average flux in an elliptical annuli centred on the object excluding other detected sources to obtain the flux as a function of radius. Once the slope levels off, it determines the sky from the last few annuli.

In the following, we use as primary size estimator the circularized effective radius defined by

$$R_{\text{eff}} = r_e \times \sqrt{b/a}. \quad (1)$$

The accuracy of our size estimates is assessed through extensive simulations in which we drop mock galaxies in real background images. The background is built as a composite image of empty regions distributed in all the fields. We generate 3000 galaxies with random magnitudes in the range  $20 < z_{850} < 26$  mag, and a Sérsic profile with random effective radii, Sérsic indices and ellipticities. These properties are taken randomly following the real distributions: effective radius distribution peaks at  $\langle r_e \rangle = 0.4$  arcsec with a dispersion of  $\sigma_{r_e} = 0.24$ , Sérsic indices peaks at  $\langle n \rangle = 3.7$  with  $\sigma_n = 1.5$ ,  $\langle e \rangle = 0.67$  with  $\sigma_e = 0.17$  and magnitudes peaks at  $z_{850} = 24$  mag with  $\langle z_{850} \rangle = 1.5$ . A Poisson noise is added and the simulated galaxy is convolved with a PSF. We then run GALAPAGOS on the mock data set and compare the output and input parameters. Results are shown in Fig. 5 and Table 3 as a function of the input surface brightness,  $\mu_{\text{in}} = \text{mag}_{\text{in}} + 2.5 \log(2\pi r_{e,\text{in}}^2)$  mag arcsec $^{-2}$  for the  $z_{850}$ -band images. Our main conclusion after inspection of Fig. 5 is that results are robust for objects brighter than 24 mag arcsec $^{-2}$ . Sizes can be recovered with a systematic error lower than 10 per cent and a dispersion lower than 30 per cent up to  $\mu = 24$  mag arcsec $^{-2}$  (see Table 3 for errors details). Similar conclusions hold when the  $i_{775}$  band is used instead of the  $z_{850}$  band.

Since the size measurements are very sensitive to the sky estimate, especially in dense regions such as clusters we double checked the robustness of our size estimates by running GALFIT a second time with a sky value estimated with the method described in Raichoor et al. (2012). In that work, the fitting procedure simultaneously fits any object closer than 2.5 arcsec from the considered ETG. The method was designed for cluster (hence crowded) environments. Moreover, the sky is fixed during the fit: it is set to a value robustly estimated on a 20 arcsec  $\times$  20 arcsec stamp. For more information, the method is detailed in section 3.1 of Raichoor et al. (2012). We find that both methods deliver consistent size measurements at 1 $\sigma$  level.

### 2.4 Stellar masses

We estimate stellar masses of our galaxies through spectral energy distribution (SED) fitting using the spectral library of Bruzual & Charlot (2003, hereafter, BC03) with the LEPHARE code (Arnouts

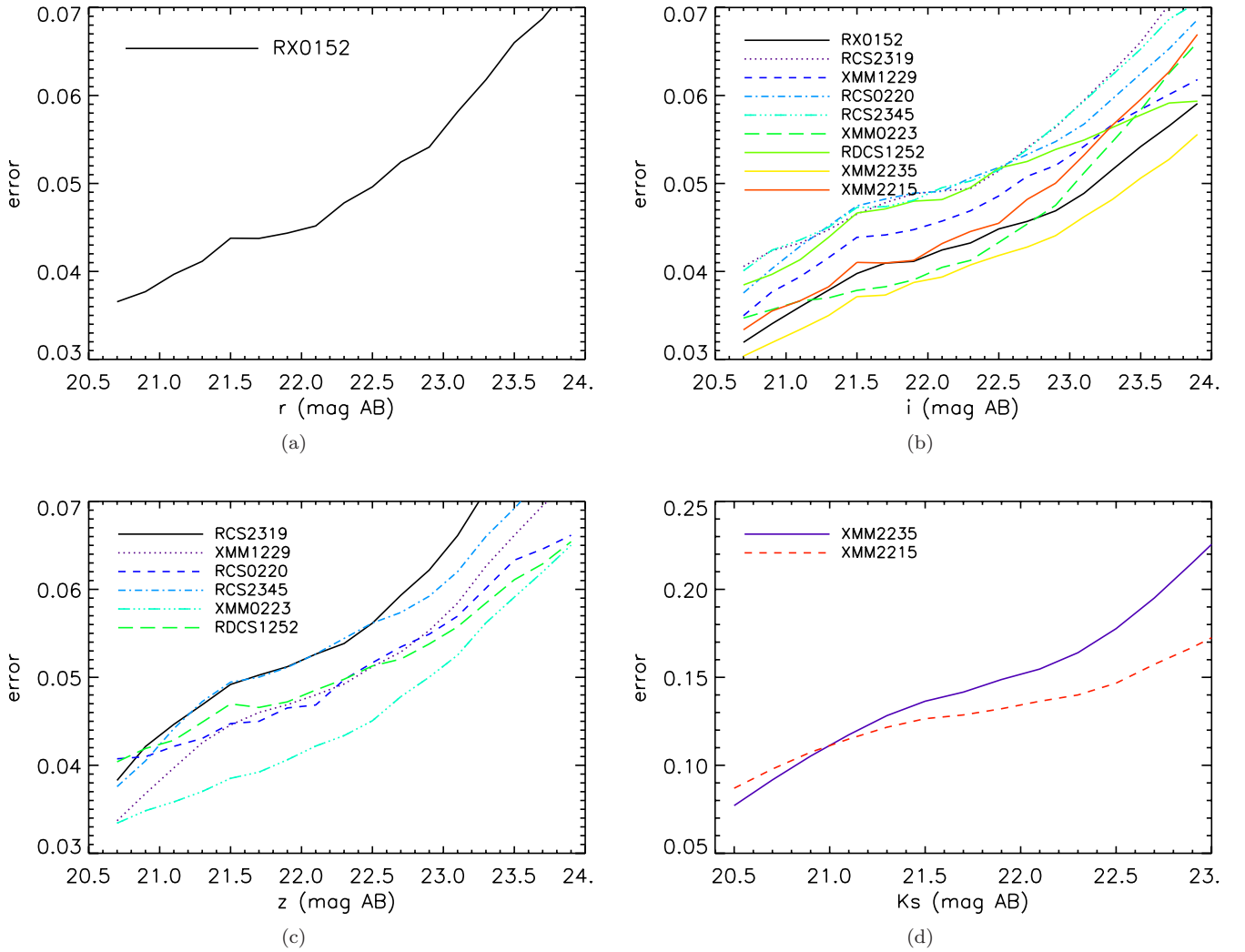


**Figure 3.** Photometric uncertainties estimated by adding artificial galaxies to the images. The errors correspond to  $1\sigma$  of the distribution of the difference between the input and recovered magnitudes.

et al. 1999; Ilbert et al. 2006). We consider galaxy templates from stellar population models with a Chabrier (2003) IMF, three different metallicities ( $Z = 0.004$ ,  $Z = 0.008$  or  $Z = 0.02$ ), exponentially declining star formation histories (SFH)  $\psi(t) \propto e^{-t/\tau}$  with a characteristic time  $0.1 \leq \tau$  (Gyr)  $\leq 30$ , and no dust extinction. The redshift of the galaxy is fixed to the cluster redshift before performing the fit, to avoid degeneracies between redshift and stellar mass. We use MAG\_AUTO magnitudes in all available filters ( $i$ ,  $z$ ,  $J$  and  $K$  for all clusters except RX0152, which used  $r$ ,  $i$ ,  $z$  and  $K$ ) with errors estimated as explained in Section 2.2.

## 2.5 Morphologies

Deriving morphologies of  $z > 1$  galaxies remains a challenge even with the high spatial resolution delivered by the *HST*. Therefore, in this work, we estimate  $B$ -rest-frame morphologies visually and with an automated method. We only derive morphologies for galaxies with  $z_{850} < 24$  mag since a visual inspection and also preliminary tests with our automated algorithms indicate that galaxies fainter than this magnitude have a signal-to-noise ratio too low to derive reliable classifications (see also, e.g. Postman et al. 2005).

### 2.5.1 Automated morphologies

For the automated morphological classification, we use GALSVM, a non-parametric code based on support-vector machines (Huertas-Company et al. 2008, 2009, 2011). The code follows a Bayesian approach to associate a probability to each galaxy to be of a given morphological type, previously defined by the user. GALSVM is trained on a local sample with known visual morphologies chosen at the same rest-frame band than the high-redshift sample. The training set is then moved at high redshift (which includes image degradation, resampling, etc.) and dropped in the high- $z$  real background. The code measures afterwards a set of morphological parameters (asymmetry, concentration, smoothness, etc.) on the simulated data set and trains a support-vector machine. During the classification process, possible systematic errors detected in the testing step are taken into account. The local sample used in this work is a catalogue from the Sloan Digital Sky Survey DR7 of about 14 000 galaxies visually classified (Nair & Abraham 2010). We refer the reader to Pović et al. (2013) for more details on how the stamps of the local galaxies were produced. For each cluster, we took a sample of 3500 galaxies and used 3000 for training and 500 to estimate errors.

In this work, galaxies are classified into three morphological classes (ellipticals, lenticulars and spirals/irregulars). We refer the

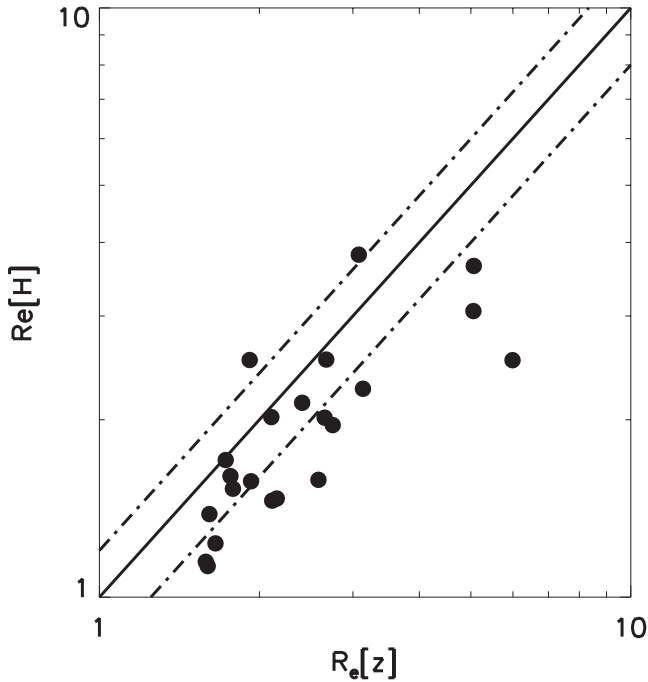


**Figure 4.** Comparison of sizes derived in the  $H$  band and  $z$  band for galaxies in cluster XMM1229 at  $z \sim 1$ . The dash-dotted lines show the 20 percent lines. We measure an  $\sim 20$  percent systematic difference with 20 percent scatter.

reader to Huertas-Company et al. (2013b) for more details on how these classes are defined. However, in the following we will only focus on ETGs (including ellipticals and lenticulars) defined as those objects with  $P(\text{ETG}) > 0.5$  (some example stamps are shown in Fig. 6).

**Table 3.** Bias and dispersions in the results of simulated quantities ( $r_e$ , mag,  $n$ ) for different surface brightness bins (left-hand column).

bin $\mu_{in}$	$n_{\text{obj}} - 3\sigma$	$\langle \delta r_e \rangle$	$\sigma(\delta r_e)$	$\langle \delta \text{mag} \rangle$	$\sigma(\delta \text{mag})$	$\langle \delta n \rangle$	$\sigma(\delta n)$
[18, 20]	175	-0.08	0.16	0.04	0.04	-0.19	0.12
[20, 22]	674	-0.05	0.12	0.02	0.05	-0.14	0.12
[22, 24]	1307	0.02	0.30	-0.01	0.17	-0.09	0.28
[24, 26]	903	0.12	0.64	-0.04	0.36	-0.08	0.43
[26, 28]	78	-0.21	0.44	0.12	0.40	-0.35	0.36

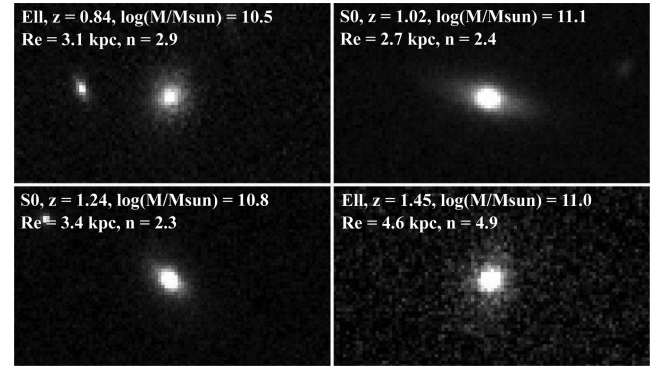


**Figure 6.** Image stamps of ETGs in four different clusters obtained from *HST/ACS* images.

### 2.5.2 Visual morphologies

Three of us (LD, MHC and SM) also visually classified all the sample in the same three morphological classes (elliptical, lenticular and spiral/irregular). For the final visual classification, we only keep objects for which at least two classifiers agree. General good agreement is found between visual and automated classification of ETGs, i.e. we measure between 2 and 15 percent disagreement

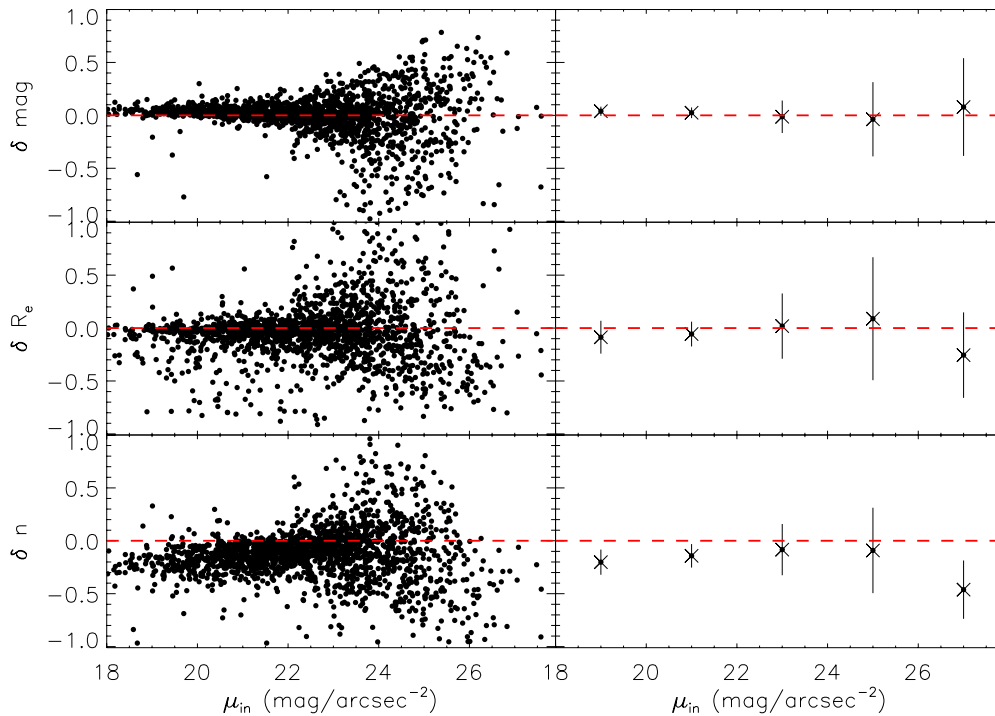


**Figure 5.** Left-hand panel: difference between the recovered and input magnitudes, effective radii and Sérsic indexes as function of the input surface brightness magnitude  $\mu_{in}$ . Right-hand panel: mean value and standard deviation of the difference in bins of size  $\delta m = 2$ . A  $3\sigma$  clipping method was applied.

**Table 4.** Number of galaxies in the final sample of the nine clusters with  $\log(M/M_{\odot}) > 10.5$  and  $z_{850} < 24$ . No. of ETGs without  $z$ : total number of ETGs without spectroscopic redshift on the red sequence (RS) with  $P(\text{ETG}) > 0.5$ . No. of ETGs with  $z$ : total number of ETGs with spectroscopic redshift on the RS with  $P(\text{ETG}) > 0.5$ . Contamination: percentage of spectroscopically confirmed outliers from cluster among ETGs on the RS (number of galaxies). No. of bad fits: number of ETGs for which GALFIT does not converge. No. of LTGs: percentage of misclassified late-type galaxies by GALSVN (number of clear LTGs + number of uncertain LTGs). No. of E-S0: percentage of disagreement between visual and automated GALSVN classification of E and S0 galaxies.

Cluster	No. of ETG without $z$	No. of ETG with $z$	Contamination	No. of bad fits	No. of LTGs	No. of E-S0
RXJ0152	49	44	14 per cent (7)	4	4–6 per cent (4+2)	30 per cent
RCS2319	20	11	35 per cent (6)	2	6–12 per cent (2+2)	36 per cent
XMMJ1229	24	15	15 per cent (2)	0	3–8 per cent (1+2)	21 per cent
RCS0220	28	5	– (0)	0	9–15 per cent (3+2)	31 per cent
RCS2345	12	12	20 per cent (3)	0	0–4.5 per cent (0+1)	23 per cent
XMMJ0223	12	19	5 per cent (1)	0	10 per cent (3+0)	32 per cent
RDCSJ1252	4	25	14 per cent (4)	0	4 per cent (1+0)	31 per cent
XMMU2235	3	10	41 per cent (7)	0	0–8 per cent (0+1)	15 per cent
XMMJ2215	12	8	20 per cent (2)	0	5–15 per cent (1+2)	20 per cent

(depending on the cluster – see Table 4), which corresponds to an average of  $5 \pm 2$  per cent discrepancy in the whole cluster ETGs selection.

The level of discrepancy between ellipticals and lenticulars visually and automatically classified is logically higher and reaches  $\sim 30$  per cent. Interestingly, this is roughly the same level of agreement expected between two independent human classifiers (see also Postman et al. 2005).

We also compared our morphologies to published results. Two of the clusters (XMM1229 and XMM2215) have indeed available visual morphologies for some objects which we have compared to our automated determination:

(i) Santos et al. (2009) visually classified 26 galaxies in XMM1229. Our automated classification agrees at an 85 per cent level with their results. Only four galaxies have an associated probability smaller than 0.5 and are visually classified as ETGs by Santos et al. (2009).

(ii) A similar study was done in XMM2215, the most distant cluster in our sample at  $z = 1.45$ , by Hilton et al. (2009) who visually classified 36 galaxies with  $z_{850} < 24$  mag. For that particular data set, we find that 22 per cent (eight galaxies) of the objects have different classifications. A similar level of disagreement (14 per cent, five) is however measured between our visual classification and the published one.

We will discuss how the differences between the different morphological classifications affect our main results in Section 4.4.

## 2.6 Sample selection

In the remaining of this work, we will consider only galaxies with  $z_{850} < 24$  mag in order to have accurate size estimates and morphologies (see Sections 2.3 and 2.5). Several further selections to build our final sample of cluster members are done, which are detailed in the following.

(i) Since we are interested in passive ETGs, we use the red sequence to determine cluster members when no spectroscopic redshift is available. We therefore selected objects belonging to the cluster according to their position in the observed colour–magnitude plane closer to the rest frame ( $U - B$ ) versus  $B$  plane. The magnitudes used change therefore from cluster to cluster depending on the redshift (Fig. 7). Colours are measured as explained in Section 2.2, i.e. within an aperture of one effective radius. For each cluster, we

then fit a linear red sequence (colour =  $a + b \times \text{mag}$ ), using only spectroscopically confirmed members and then select cluster members within  $3\sigma$  of the best fit (Fig. 7). The fit is performed with an iterative sigma-clipping linear regression and the scatter  $\sigma$  is computed with a robust standard deviation based on bi-square weights (Tukey’s biweight; Press et al. 1992). We measure a fraction of outliers, corresponding to the fraction of galaxies with a spectroscopic redshift outside the cluster, between 5 and 20 per cent (see details in Table 4), which are removed from the final selection. Only two clusters, RCS2319 and XMM2235, have larger contaminations (31 and 44 per cent, respectively).

An alternative to the red-sequence-based selection is a selection based on photometric redshifts, which has in principle the advantage of selecting all members independently of their star formation activity. We therefore obtained photometric redshifts for all the detected sources through SED fitting with two different codes: LEPHARE (Arnouts et al. 1999; Ilbert et al. 2006) and EAZY (Brammer, van Dokkum & Coppi 2008) using the filters specified in Table 1 for each cluster. For LEPHARE, we used synthetic galaxy templates from BC03 models with a Chabrier (2003) IMF, three different metallicities ( $Z = 0.004$ ,  $Z = 0.008$  or  $Z = 0.02$ ), exponentially declining SFH  $\psi(t) \propto e^{-t/\tau}$  with a characteristic time  $0.1 \leq \tau$  (Gyr)  $\leq 30$ , and no dust extinction (e.g., Ilbert et al. 2006). For EAZY, we kept default settings and a  $K$ -band magnitude prior. We then consider that a galaxy belongs to a given cluster if  $|z_{\text{phot}} - z_{\text{cluster}}| < \Delta z$  with  $\Delta z$  changing from cluster to cluster to maximize the completeness and minimize the contamination simultaneously based on the spectroscopic sample only as described in Pelló et al. (2009). When no colour pre-selection is made, the average level of contamination is very high,  $\sim 40$  per cent, which is probably due to the fact that our sample lacks of blue filters. If instead, we restrict to red galaxies by applying a colour cut ( $r_{625} - i_{775} > 0.8$ ,  $i_{775} - z_{850} > 0.5$  and  $i_{775} - K_s > 1.8$ ), we still find large contaminations ( $\sim 40$ – $50$  per cent) with the two algorithms for the two most distant clusters (XMM2235 and XMM2215) and a contamination around 15–35 per cent for  $z < 1.3$  clusters. These values are still larger than what is obtained with the red sequence selection, so we decided not to use photometric redshifts for selecting cluster members in this work.

(ii) Among the selected red sequence population, we then select ETGs based on our automated classifications as described in Section 2.5. A selection based on visual morphologies leads to similar results given the good agreement between the two different classifications.

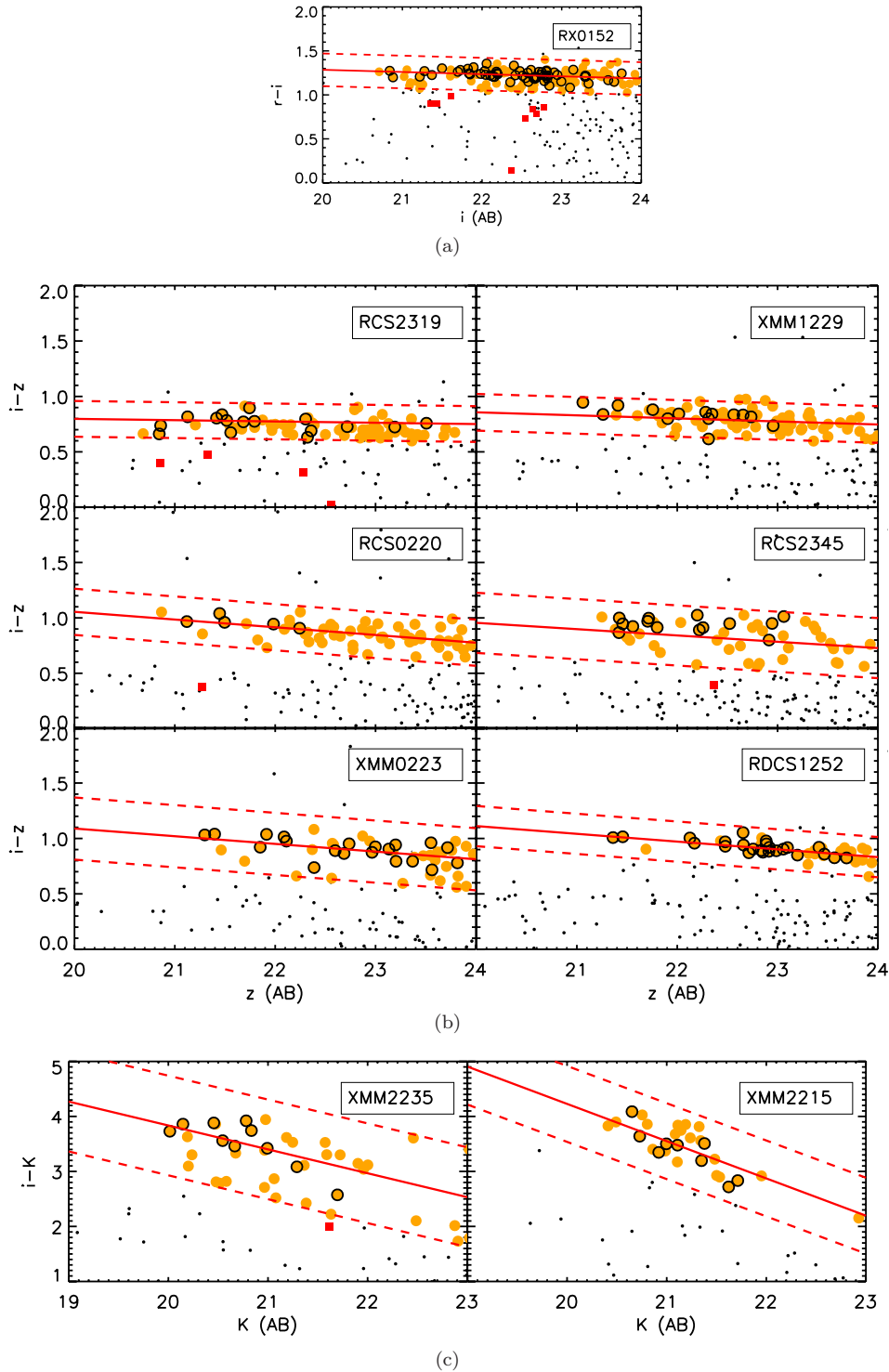


**Figure 7.** Color–magnitude diagram:  $(i_{625} - i_{775})$  versus  $i_{775}$  for RX0152 galaxies,  $(i_{775} - z_{850})$  versus  $z_{850}$  for cluster galaxies between  $z = 0.9$  and  $z = 1.23$ ,  $(i_{775} - K_s)$  versus  $K_s$  for the highest cluster galaxies at  $z = 1.39$  and  $z = 1.45$ . Orange circles with black contours correspond to ETGs with spectroscopic redshift in the cluster used to fit the red sequence (red line). Red dashed lines correspond to the fitted red sequence at  $\pm 3\sigma$ . Orange circles correspond to the selected ETGs on the red sequence  $\pm 3\sigma$ . Red squares are for ETGs with spectroscopic redshift in the cluster, but not on the red sequence.

(iii) We also remove objects for which the Sérsic fits did not converge (see Section 2.3 for size determination method). We consider that the fitting procedure has converged if  $\text{mag} \leq 24$ ,  $|M_{\text{galfit}} - M_{\text{SEx}}| < 0.8$ ,  $0.1 < R_{\text{eff}} < 1.6$  arcsec and  $n \neq 8$ . We obtain less than 1 per cent non-converged fits for cluster ETGs selected on the red sequence with  $\log(M/M_{\odot}) \geq 10.5$  and  $z_{850} < 24$  mag.

Exact numbers are detailed in Table 4. This number is negligible compared to the total number of selected passive ETGs, so it has no impact in our results.

(iv) Finally, we keep only ETGs with a stellar mass greater than  $3 \times 10^{10} M_{\odot}$  to keep a complete sample. We used two different approaches to estimate the mass completeness. First, following

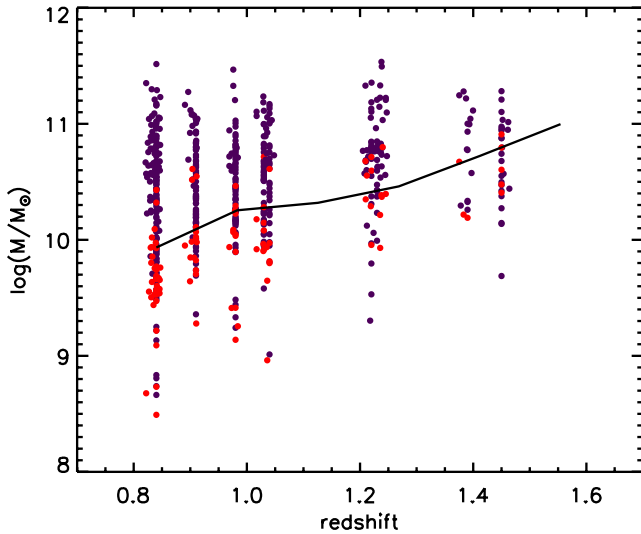
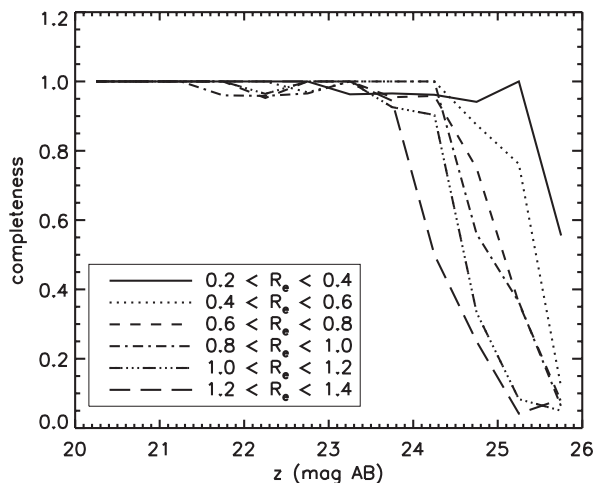
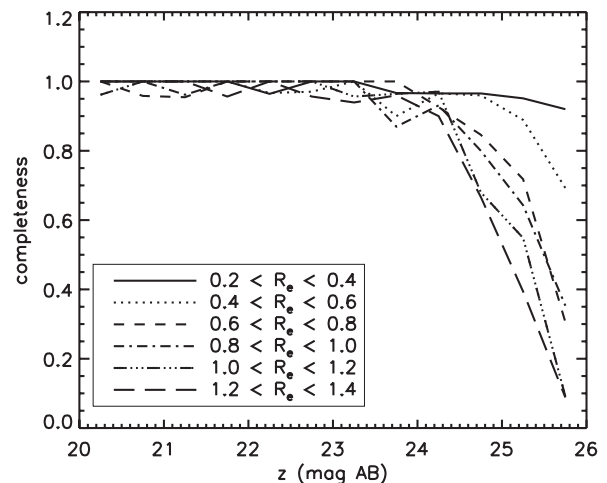


**Figure 8.** Stellar mass as a function of redshift of the HCS ETG sample in the  $z$ -band images. Red dots are  $M^{\text{lim}}$  and the black line shows the 80 per cent completeness level (Pozzetti et al. 2010).

Pozzetti et al. (2010), for each passive ETG with spectroscopic redshift, we compute the limiting stellar mass ( $M^{\text{lim}}$ ) given by  $\log(M^{\text{lim}}) = \log(M) - 0.4(z_{850} - z_{\text{lim}})$ , where  $z_{\text{lim}} = 24$  mag in our case. We use the limiting mass of the 20 per cent faintest galaxies at each cluster redshift and estimate that way the mass limit at 80 per cent completeness. As shown in Fig. 8, our sample is 80 per cent complete for galaxies with stellar mass greater than  $\log(M/M_{\odot}) = 10.2$  at  $z \sim 1$  and  $\log(M/M_{\odot}) = 10.8$  at  $z \sim 1.45$ . Secondly, we used an approach similar to Bundy et al. (2010) and estimated the apparent magnitude in the  $z$  band of a typical passive galaxy using stellar population models (i.e. solar metallicity and no dust and with a  $\tau = 0.5$  Gyr burst of star formation occurring at  $z_f = 5$ ). At  $z = 1.45$ , the redshift of the most distant cluster, a galaxy of  $z_{850} = 24$  mag has a stellar mass of  $\log(M/M_{\odot}) = 10.7$ , which is roughly consistent with the estimate. We also make sure that, with the depth of our images, we detect >90 per cent of the galaxies with  $z_{850} < 24$  mag through simulations independently of their size (Fig. 9).



(a)



(b)

**Figure 9.** Completeness of the HCS sample in the  $z$ -band images as a function of magnitude and size (in arcsec) – left-hand panel: for the least deep image (RCS2319) and right-hand panel: for a typical image depth of HCS (here, XMM1229).

The final cluster sample contains 313 cluster galaxies, among which 149 are spectroscopically confirmed members. Details are given in Table 4.

### 3 FIELD COMPARISON SAMPLE

In order to disentangle the environmental effects on the size evolution of passive ETGs, we define a field sample from a combination of four different data sets to be compared with our main cluster sample.

(i) A first set of galaxies is built by putting together all foreground and background galaxies detected in the clusters fields with spectroscopic redshifts ( $|z - z_{\text{cl}}| > 0.02$ ) in the redshift range  $0.7 < z < 1.6$ . We then apply the same colour selection than for cluster galaxies (see Section 2.6). This ensures a subsample with exactly the same properties in terms of resolution and depth than the main cluster sample. All derived quantities (stellar masses, sizes and morphologies) are therefore obtained with the same methods described for the cluster sample in Section 2. This first field sample is referred in the following as the *HCS field sample* and contains 30 galaxies.

(ii) To increase the number of field galaxies, we add a sample of galaxies from the COSMOS survey (Scoville et al. 2007, referred in the following as *the COSMOS sample*) with photometric redshifts between  $z = 0.7$  and 1.6 from George et al. (2011) and sizes from Huertas-Company et al. (2013b). Passive galaxies are selected using the colour selection  $\text{NUV} - R > 3.5$  (Ilbert et al. 2010) corrected for dust extinction where NUV is the near-ultraviolet band from *GALEX* and  $R$  is an optical band from Subaru Telescope. Sizes are estimated using also *GALAPAGOS* on the *HST/ACS F814W* ( $i$ -band) images as described in Huertas-Company et al. (2013b). Since galaxies in the COSMOS sample are selected based on the  $i$ -band magnitude ( $i < 24$ ), we have checked the reliability of the size estimates in the redshift range explored by carrying out similar simulations as we did for the cluster ETGs. We find comparable results for the HCS objects brighter than  $z_{850} = 24$  mag (i.e. systematic error lower than 0.1 and a reasonable scatter lower than 0.2 up to  $i < 24$  mag; Huertas-Company et al. 2013b). However, the  $i$ -band selection implies a mass completeness close to  $10^{11} M_{\odot}$  at  $z \sim 1.5$  (extrapolation of fig. 4 of Huertas-Company et al. 2013b), and the COSMOS sample is therefore less complete than our main cluster

sample (see Section 2.6). We will discuss the effects of this when discussing our main results. Stellar masses are estimated using the LEPHARE software with BC03 library and a Chabrier IMF with all the available filters in COSMOS with the same parameters used for the HCS cluster and field samples. Our stellar mass estimates show in fact a small shift (0.2 dex) when compared to the Bundy et al. (2006) stellar mass estimates used in George et al. (2011). These small shifts are common when comparing stellar masses used with different algorithms and settings. Finally, morphologies were derived automatically (see Huertas-Company et al. 2013b) and visually by two of us (LD and MHC) following the same methodology that was adopted for the main sample. The whole COSMOS sample contains 211 galaxies.

(iii) Additional field galaxies in the redshift range  $1.1 < z < 1.4$  with published sizes, stellar masses and morphologies (Raichoor et al. 2012) from the GOODS-CDF-S field (Giavalisco et al. 2004) are also considered (*GOODS sample* in the following). The sample is selected from the public GOODS-MUSIC v2 catalogue (Santini et al. 2009) and at  $z_{850} = 24$  mag, the sample is more than 70 per cent complete. We select only red galaxies with  $0.75 < i - z < 1.1$ . All these galaxies have a spectroscopic redshift. We refer to Raichoor et al. (2011) for a detailed description of the selection and for further information about the completeness of the sample. Stellar masses in the GOODS-S sample were measured with an SED fitting code (different from LEPHARE) using BC03 stellar population models and a Salpeter IMF (see Raichoor et al. 2011 for details). To convert into a Chabrier IMF, we applied the following correction:  $\log(M_{\text{Chabrier}}) = \log(M_{\text{Salpeter}}) - 0.25$  taken from Bernardi et al. (2010). We have checked that the resulting stellar masses are consistent at  $1\sigma$  level with the ones obtained with LEPHARE. Sizes were computed on the *HST/ACS*  $z_{850}$  image using GALFIT with a fixed sky value previously derived on a larger stamp centred on the ETG (see section 3 of Raichoor et al. 2012 for more details on the method). Finally, galaxies were visually classified (E/S0 types) in the *HST/ACS F850LP* images as described in Mei et al. (2012). This sample contains 17 galaxies.

(iv) Finally, the field sample also contains galaxies in the redshift range  $0.7 < z < 1.6$  from the CANDELS survey (Pis Faber & Jackson; see Grogin et al. 2011; Koekemoer et al. 2011) with published redshifts and sizes by Newman et al. (2012, referred in the following as *the CANDELS sample*). Sizes were also derived with GALFIT (see Newman et al. 2012 for details) in the optical rest-frame band. For consistency, we have re-computed stellar masses with LEPHARE through SED fitting using BC03 models and a Chabrier IMF in the same way as the cluster sample. We have also selected only quiescent galaxies ( $\text{SSFR} < 0.02 \text{ Gyr}^{-1}$  and no MIPS detection) and have re-assigned morphological class in the same way as for our sample. The CANDELS sample is complete for stellar masses  $\log(M/M_{\odot}) > 10.52$  with a Chabrier IMF and BC03 model [see section 2.4 of Newman et al. (2012) for details]. We have 125 galaxies in this sample.

Our final field sample contains 383 galaxies. Details are given in Table 5.

## 4 RESULTS

### 4.1 Super dense galaxies at $z \sim 1$

We study first the fraction of *compact* objects in the two different environments without morphological selection. Poggianti et al. (2013) measured a clear difference in the fraction of the so-called

**Table 5.** Number of field galaxies in the final sample with HCS and COSMOS data, GOODS sample from Raichoor et al. (2012) and CANDELS sample from Newman et al. (2012).

Redshift bin	# HCS	# COSMOS	# GOODS-S	# CANDELS
[0.7, 0.9]	9	91	–	23
[0.9, 1.1]	12	83	–	40
[1.1, 1.6]	9	37	17	62

*super dense galaxies (SDGs)* in clusters ( $\sim 20$  per cent) and in the field (4 per cent) in the local universe without morphological distinction. We compare our results at high redshift, by taking the same selection for SDGs in the same stellar mass range:

$$\Sigma_{50} > 3 \times 10^9 M_{\odot} \text{ kpc}^{-2}, \quad (2)$$

where the mean mass surface density is defined by  $\Sigma_{50} = 0.5M_{*}/\pi R_{e}^2$ , in the stellar mass range  $10.5 < \log(M/M_{\odot}) < 11.6$  with no morphological selection (all figures in this work show only ETGs). For this comparison, we restrict the cluster sample to spectroscopically confirmed members (212 galaxies) to include all morphological types in the selection (not only ETGs). The field sample is limited to the HCS sample, with 122 galaxies, because it is the only one for which the sample is not selected based on morphology. We find then 67 SDGs live in clusters ( $32_{-3}^{+4}$  per cent) and 26 SDGs in the field ( $21_{-3}^{+4}$  per cent).

The fraction of SDGs in clusters is only 1.5 larger than in the field at  $z \sim 1$ , which is three times less than the difference found by Poggianti et al. (2013) in the local Universe. Concerning the morphological properties of SDGs, we find that the fractions of late-type SDGs is  $\sim 2$  times higher in our high-redshift sample and comparable to the values measured by Valentinuzzi et al. (2010b) at similar redshifts in the ESO Distant Cluster Survey (White et al. 2005). Effective radii, Sérsic indices, axis ratios and stellar masses of our cluster and field SDGs are consistent within  $1\sigma$  with the local values of Poggianti et al. (2013). Table 6 summarizes all the properties of the SDGs found in clusters and in the field compared to the ones reported by Poggianti et al. (2013) in the local universe.

### 4.2 The MSR of ETGs in clusters at $z \sim 1$

To study the mass–size relation, we focus only on the passive ETG population. In Fig. 10, we show the MSR of passive ETGs of the nine studied clusters separately. The figure also shows the best-fitting power-law model  $\log(R_{\text{eff}}/\text{kpc}) = \kappa + \beta \times \log(M/M_{\odot})$  for each cluster with  $10.5 < \log(M/M_{\odot}) < 12$  and the best-fitting parameters are reported in Table 7.

Even though it is not the main focus of this work, we also show with a blue star in Fig. 10, for completeness, the positions in the  $M_{*} - R_{\text{eff}}$  plane of the central dominant galaxies (CDGs). CDGs are identified in this work as the closest bright galaxy to the peak of X-ray emission. As expected, these galaxies are among the most massive and largest galaxies in the cluster. We notice that for some of them (i.e. RX0152, RCS2319, XMM1229), the automated fit delivered by GALAPAGOS did not converge, so we did a new fit forcing  $n = 4$  while keeping the values obtained with the first fit for the remaining parameters. The brightest cluster galaxies (BCGs) identified in Lidman et al. (2013) as the brightest galaxies in the  $K$  band are also marked in the mass–size plane for each cluster (notice that the BCGs selected by Lidman et al. (2013) in RCS2345 and XMM0223 have a late-type morphology).

**Table 6.** SDG properties in clusters and in the field. For high-redshift SDGs, mean values are computed with  $3\sigma$ -clipping method and errors by bootstrapping. Values for local SDGs are taken from Poggianti et al. (2013).

	At $z \sim 1$		At $z \sim 0$	
	Cluster (HCS)	Field (HCS)	Cluster (WINGS)	Field (PM2GC)
$f_{\text{SDGs}}$	$32^{+4}_{-3}$ per cent	$21^{+4}_{-3}$ per cent	17 per cent	4.4 per cent
$\langle R_e \rangle$	$1.55 \pm 0.08$	$1.38 \pm 0.08$	$1.57 \pm 0.34$	$1.45 \pm 0.26$
$\langle n \rangle$	$2.98 \pm 0.13$	$2.61 \pm 0.26$	$3.1 \pm 0.8$	$2.8 \pm 0.6$
$\langle b/a \rangle$	$0.61 \pm 0.04$	$0.52 \pm 0.05$	$0.65 \pm 0.16$	$0.48 \pm 0.13$
$\langle \log(M/M_\odot) \rangle$	$10.87 \pm 0.06$	$10.90 \pm 0.05$	$10.96 \pm 4.33$	$10.78 \pm 3.41$
$f_{\text{ELL}}$	$24 \pm 6$ per cent	$15^{+11}_{-7}$ per cent	$29.1 \pm 7.8$ per cent	$22.7 \pm 7.2$ per cent
$f_{\text{S0}}$	$50 \pm 7$ per cent	$65^{+10}_{-12}$ per cent	$62.0 \pm 10.7$ per cent	$70.5 \pm 12.7$ per cent
$f_{\text{LTG}}$	$19^{+6}_{-5}$ per cent	$19^{+6}_{-8}$ per cent	$8.8 \pm 4.4$ per cent	$6.8 \pm 3.9$ per cent
$f_{\text{unknown}}$	$4^{+4}_{-2}$ per cent	–	–	–

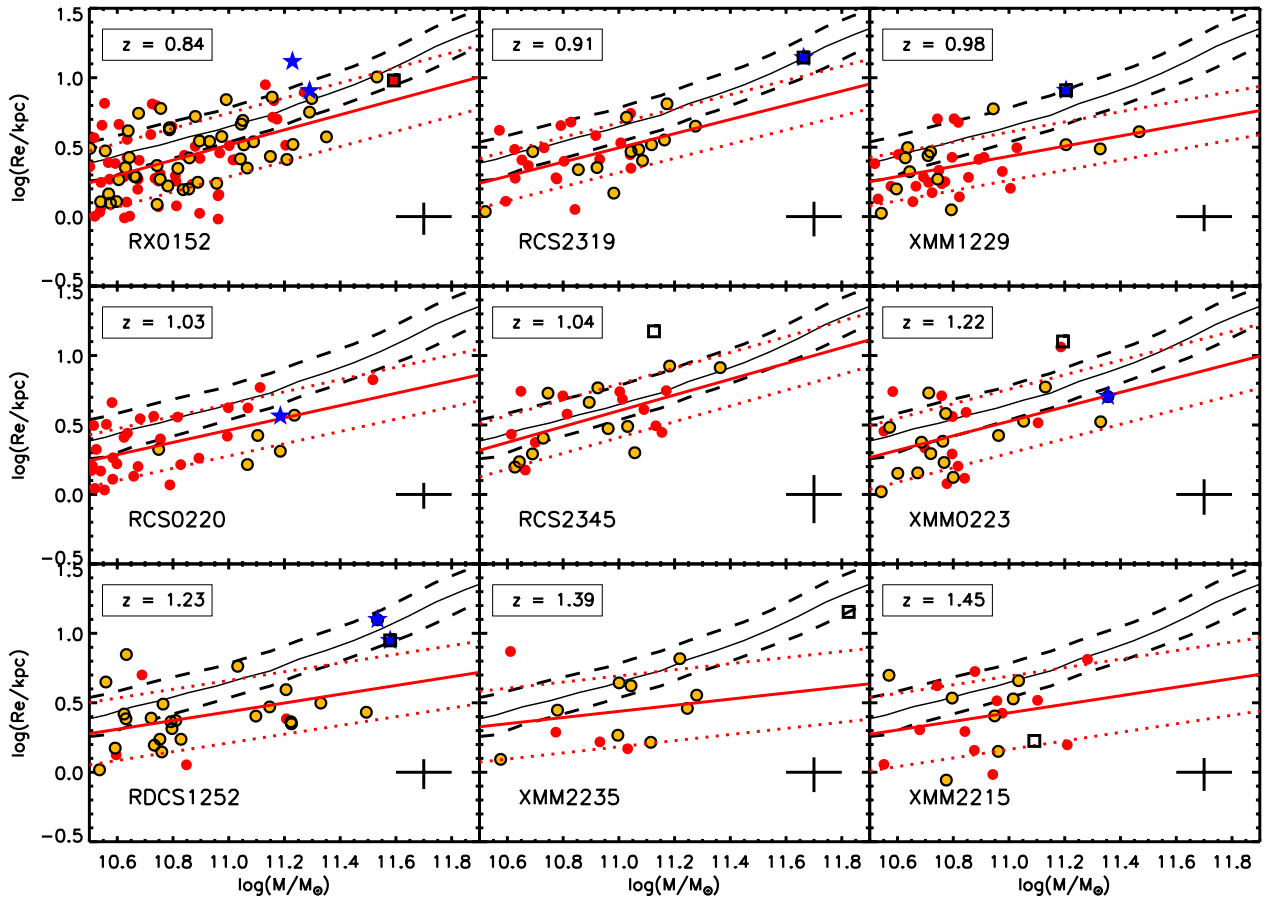


**Figure 10.** MSR of passive ETGs in clusters. Orange circles with black contour represent galaxies with spectroscopic redshift, red circles are the red sequence sample and the blue stars correspond to the CDGs we manage to identify whereas the black squares correspond to the BCGs identified by Lidman et al. (2013). The black solid line corresponds to the local relation of Bernardi et al. (2012) and the  $1\sigma$  standard deviation in black dashed lines. Each red line corresponds to the fit for each cluster sample with the  $1\sigma$  standard deviation in red dotted line. In the right end corner of each panel, the black cross represents the median error bar on mass and size.

The first result is that the slopes of the MSRs of early-type galaxies living in clusters are consistent at  $1\sigma$  up to  $z \sim 1.2$ . The typical value  $\beta = 0.49 \pm 0.08$  is also consistent with previous works without environment distinction (e.g. Cimatti, Nipoti & Cassata 2012; Newman et al. 2012). In the three most distant clusters of our sample, we measure a smaller slope  $\beta = 0.27 \pm 0.06$ , that might indicate a lack of massive and large ETGs at these higher redshifts. This difference could be due to cluster to cluster variations or a real

trend at high redshift but more statistics are required to make a firm conclusion.

We notice that the MSRs of XMM2235 and RCS1252 have already been studied in previous works (e.g. Rettura et al. 2010; Strazzullo et al. 2010), respectively. As a sanity check, we compared our MSR of XMM2235 with the one by Strazzullo et al. (2010) after applying a shift of 0.25 dex to convert from a Salpeter to a Chabrier IMF used in this work. Despite the different methods

**Table 7.** Fit parameters of the MSR for each cluster as  $\log(R_e/\text{kpc}) = \kappa + \beta \times \log(M/M_\odot)$ .

Cluster	$z_{cl}$	$\kappa \pm \Delta\alpha$	$\beta \pm \Delta\beta$	$\sigma$
RXJ0152	0.84	$-5.5 \pm 0.3$	$0.54 \pm 0.09$	0.23
RCS2319	0.91	$-5.1 \pm 0.5$	$0.5 \pm 0.1$	0.18
XMMJ1229	0.98	$-3.6 \pm 0.4$	$0.4 \pm 0.1$	0.17
RCS0220	1.03	$-4.4 \pm 0.4$	$0.4 \pm 0.1$	0.19
RCS2345	1.04	$-5.6 \pm 0.6$	$0.6 \pm 0.2$	0.19
XMMJ0223	1.22	$-5.2 \pm 0.6$	$0.5 \pm 0.2$	0.23
RDCS1252	1.23	$-3.0 \pm 0.5$	$0.3 \pm 0.1$	0.22
XMMU2235	1.39	$-2.0 \pm 1.0$	$0.2 \pm 0.3$	0.25
XMMJ2215	1.45	$-3.0 \pm 1.0$	$0.3 \pm 0.3$	0.26

used to compute sizes and stellar masses, the MSRs are consistent at  $1\sigma$ .

In the following sections, we focus on the environmental dependence of the MSR. For that purpose, we gather all passive ETGs in clusters in three redshift bins ( $0.7 \leq z < 0.9$ ,  $0.9 \leq z < 1.1$  and  $1.1 \leq z < 1.6$ ) in order to increase statistics and assume that the slope of the relation is constant in that redshift range. We therefore consider two clusters in the first bin (RX0152 and RCS2319), three clusters in the second bin (XMM1229, RCS0220 and RCS2345) and four clusters in the third bin (XMM0223, RDCS1252, XMM2235 and XMM2215).

### 4.3 The MSR of ETGs in different environments

In Fig. 11, we show the MSR of passive ETGs in clusters and in the field in the three different redshift bins described above ( $0.7 < z < 0.9$ ,  $0.9 < z < 1.1$  and  $1.1 < z < 1.6$ ) and summarize the best-fitting parameters using a power law in Table 8.

In order to look for differences in the intercepts ( $\kappa$ ) of field and cluster MSRs, we fix the slope at  $\beta = 0.57$  (the value measured in the local universe and compatible with our measurements) and perform a new fit. Cluster galaxies tend to present larger intercept values with the difference increasing with redshift. In fact, the percentage difference goes from 9 per cent at  $z \sim 0.8$  to 23 per cent at  $z \sim 1.5$ . The latter is significant at more than  $3\sigma$ . This result suggest that cluster red sequence ETGs are on average larger than field galaxies at fixed stellar mass. We precisely quantify this effect in Section 4.4. We emphasize that this result is not in contradiction with the fact that there is a larger fraction of SDGs in clusters since the analysed populations are different (there is no morphological selection for SDGs).

### 4.4 Size evolution of massive ETGs in different environments

We now focus on the size evolution over the  $\sim 2.5$  Gyr covered by our data. We will use in the following as primary size estimator the mass-normalized size ( $\gamma$ ) as defined by Newman et al. (2012) and Cimatti et al. (2012):

$$\gamma = R_e/M_{11}^\beta \quad (3)$$

with

$$M_{11} = M_*/10^{11} M_\odot \quad (4)$$

and

$$\beta = 0.57. \quad (5)$$

By using this quantity we intentionally remove the correlation between  $R_e$  and  $M_*$  which could produce spurious differences in the

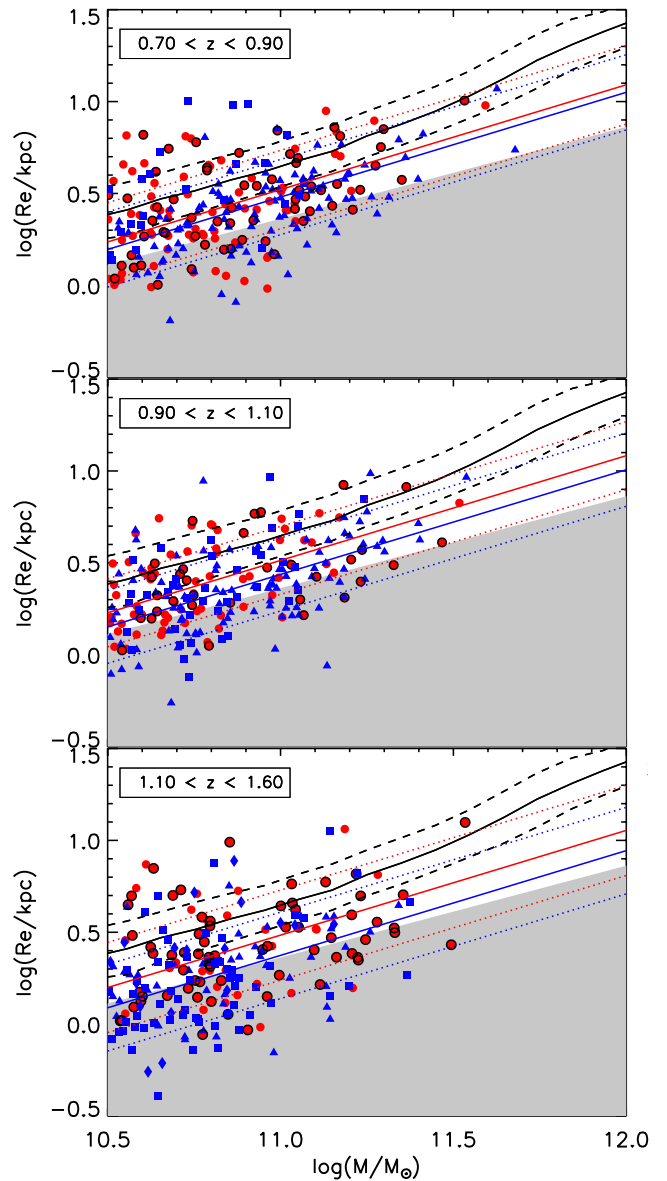


**Figure 11.** MSR of passive ETGs in clusters and in the field. The local MSR of Bernardi et al. (2012) is represented in black lines. Passive ETGs in clusters are represented in red circles and passive ETGs in the field are the blue symbols. Blue squares are from the CANDELS sample of Newman et al. (2012) and blue diamonds are the GOODS sample from Raichoor et al. (2012). Symbols circled in black are spectroscopically confirmed cluster members. Blue and red lines correspond, respectively, to the fit of the MSR with a fixed slope for field sample and for cluster sample and the dotted lines, the fit  $\pm 1\sigma$ . The shaded region shows the area occupied by SDGs (see the text for details).

size distributions of different samples if the mass distributions are not identical. This is basically equivalent to following the evolution of the intercept on the MSR, once the slope is fixed. The  $\beta$  parameter is calibrated on the local MSR and the main assumption we make is that the slope of the relation does not change significantly with redshift which, as shown in the previous section, is consistent with our sample at first level. We notice that our main results are robust against changes in  $\beta$  of around 10 per cent.

We first show in Fig. 12 the  $\gamma$  distributions in three redshift bins, in clusters and in the field. In some redshift bin, Kolmogorov–Smirnov (KS) tests present small values (see Table 9), but never

**Table 8.** Fit parameters of the MSR for field and cluster galaxies as  $\log(R_e/\text{kpc}) = \kappa + \beta \times \log(M/M_\odot)$  with free slope and fixed slope  $\beta = 0.57$ .

Redshift	Environment	$\kappa \pm \Delta\kappa$	$\beta \pm \Delta\beta$	$\sigma$
[0.7, 0.9]	Cluster	$-5.2 \pm 0.3$	$+0.52 \pm 0.08$	0.22
	Field	$-4.7 \pm 0.2$	$+0.47 \pm 0.07$	0.19
	Cluster	$-5.75 \pm 0.02$	$+0.57$	0.21
	Field	$-5.79 \pm 0.02$	$+0.57$	0.20
[0.9, 1.1]	Cluster	$-4.8 \pm 0.3$	$+0.48 \pm 0.08$	0.19
	Field	$-5.8 \pm 0.2$	$+0.57 \pm 0.07$	0.19
	Cluster	$-5.75 \pm 0.02$	$+0.57$	0.18
	Field	$-5.83 \pm 0.02$	$+0.57$	0.20
[1.1, 1.6]	Cluster	$-3.3 \pm 0.3$	$+0.34 \pm 0.10$	0.25
	Field	$-5.2 \pm 0.3$	$+0.50 \pm 0.10$	0.24
	Cluster	$-5.78 \pm 0.03$	$+0.57$	0.24
	Field	$-5.89 \pm 0.02$	$+0.57$	0.23

low enough ( $P < 0.05$ ), to clearly state that the two distributions are different.

In order to estimate the mean sizes at a given redshift, the size distributions for cluster and field galaxies are fitted with a model in which  $\log(\gamma)$  follows a skew-normal distribution, as previously done by Newman et al. (2012). The best-fitting models are overplotted in Fig. 12.

This model has the advantage of better describing eventual asymmetries in the size distribution. The skew normal distribution has indeed three parameters: the mean ( $\log(\gamma)$ ), the standard deviation  $\sigma_{\log(\gamma)}$ , and a shape parameter  $s$  that is related to the skewness:

$$P(\log(\gamma)) = \frac{1}{\omega\pi} e^{-\frac{(\log(\gamma)-\psi)^2}{2\omega^2}} \int_{-\infty}^{s\frac{\log(\gamma)-\psi}{\omega}} e^{-\frac{t^2}{2}} dt. \quad (6)$$

We then estimate  $\langle \log(\gamma) \rangle$  at a given redshift as the mean of the best-fitting skew normal distribution, which is given by  $\langle \log(\gamma) \rangle = \psi + \omega\delta\sqrt{2/\pi}$  where  $\delta = s/\sqrt{1+s^2}$ . Uncertainties on sizes are then computed by bootstrapping, i.e. we repeat the computation of each value 1000 times taking a random subset of the data each time, and compute the error as the scatter of all the measurements.

Fig. 13 shows now the redshift evolution of  $\langle \log(\gamma) \rangle$  for passive ETGs in clusters and in the field with stellar masses above  $3 \times 10^{10} M_\odot$ . Cluster ETGs have mean values of  $\langle \log(\gamma) \rangle \sim 1.3$  times larger than field ETGs of the same stellar mass (see also Tables 10 and 11). We notice that the position of the peaks of the distributions of clusters and field galaxies in Fig. 12 (mode values

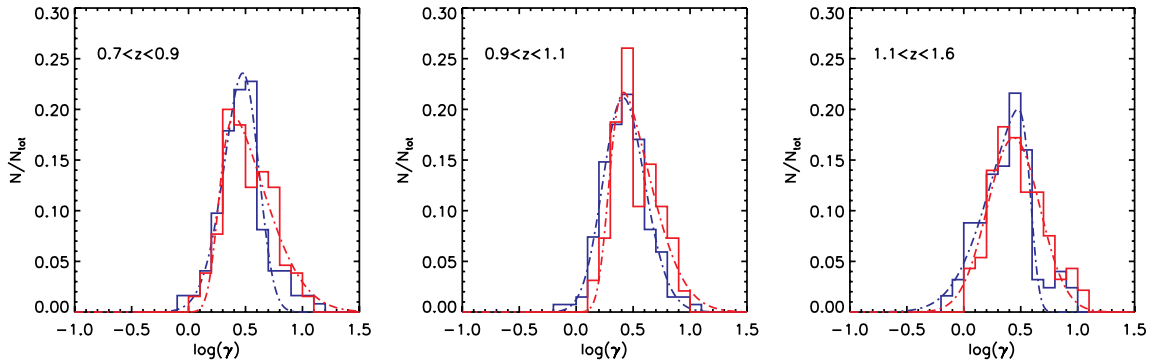


**Figure 12.** Distributions of  $\log(\gamma)$  of passive ETGs with  $\log(M/M_\odot) \geq 10.5$  in the field (blue dashed line) and in clusters (red line) for three bins of redshifts. The red line and blue dashed line show the best-fitting skew normal distribution for cluster and field galaxies, respectively. Galaxies in clusters show a population of galaxies with larger sizes that are not found in the field (see the text for details).

**Table 9.** Results of KS and Kuiper statistical tests applied to field and cluster ETGs mass-normalized radius distributions for different redshift bins.  $N_{\text{cluster}}$  and  $N_{\text{field}}$  indicate, respectively, the number of cluster galaxies and the number of field galaxies in each sample.

Mass	Redshift	$N_{\text{cluster}}$	$N_{\text{field}}$	KS	Kuiper
$\log(M/M_\odot) \geq 10.5$	$0.7 \leq z < 0.9$	130	123	0.05	0.14
	$0.9 \leq z < 1.1$	96	135	0.06	0.25
	$1.1 \leq z < 1.6$	94	125	0.03	0.29

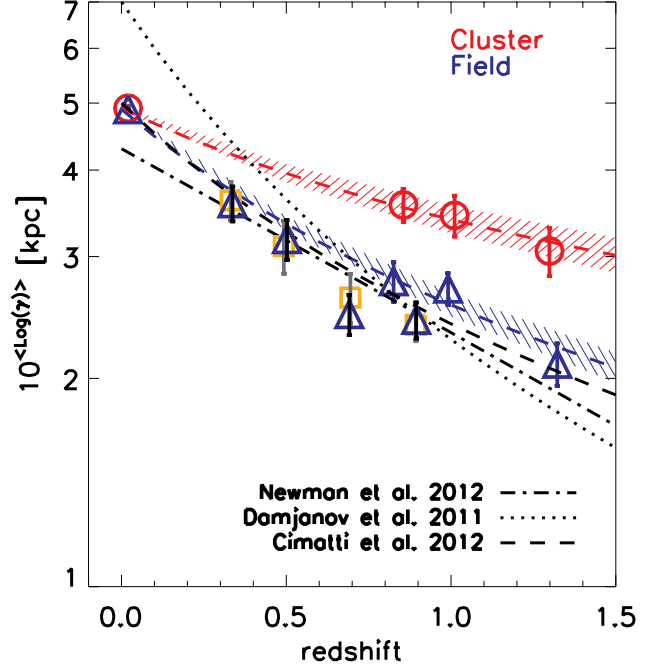


**Figure 13.** Evolution of  $\langle \log(\gamma) \rangle$  for passive ETGs with  $\log(M/M_\odot) \geq 10.5$  in clusters (red circles) and in the field (blue triangles). The points at  $z = 0$  show the value of  $\langle \log(\gamma) \rangle$  in the local universe in clusters and in the field, respectively (see the text for details). The number of objects in each redshift bin is shown in Table 10. Black squares and diamonds are the values in the field and in groups from Huertas-Company et al. (2013b). Blue and red dashed lines show the best-fitting model  $\gamma \propto (1+z)^\alpha$  for field and cluster galaxies respectively. Cluster passive ETGs are on average larger at  $z \sim 1$  and present a less steep evolution than field galaxies at fixed stellar mass. We notice that the Newman et al. (2012) line has been shifted by  $-0.07$  dex respect to the published version to account for differences in IMF (Salpeter versus Chabrier) as well for the different methodologies used to compute sizes and select passive galaxies.

**Table 10.** Mean, mode and median values of  $\log(\gamma)$  in linear scale ( $10^{\log(\gamma)}$ ) measured in our sample from the best-fitting skew normal distribution (see the text for details) and for different selections. The median of the distribution obtained directly on the data is also shown (median-no fit column).

Redshift bin	All Q-ETGs											
	<i>N</i>	Mean	Clusters		Field		Median (no fit)	<i>N</i>	Mean	Mode	Median	Median-no fit
[0.7, 0.9]	130	3.56 ± 0.20	2.52 ± 0.54	3.22 ± 0.17	3.10 ± 0.16	123	2.76 ± 0.18	2.99 ± 0.55	2.83 ± 0.12	3.00 ± 0.12		
[0.9, 1.1]	96	3.44 ± 0.23	2.61 ± 0.35	3.22 ± 0.20	3.00 ± 0.19	135	2.70 ± 0.14	2.58 ± 0.30	2.66 ± 0.11	2.66 ± 0.12		
[1.1, 1.6]	93	3.06 ± 0.24	2.40 ± 0.41	2.85 ± 0.19	2.79 ± 0.20	125	2.10 ± 0.15	2.98 ± 0.50	2.31 ± 0.13	2.46 ± 0.19		
$M_*/M_\odot > 10^{11}$												
[0.7, 0.9]	36	3.35 ± 0.33	1.79 ± 1.44	3.03 ± 0.42	3.12 ± 0.41	40	2.70 ± 0.19	2.63 ± 0.57	2.69 ± 0.17	2.91 ± 0.24		
[0.9, 1.1]	23	3.11 ± 0.39	2.17 ± 1.24	2.81 ± 0.41	2.73 ± 0.40	42	2.69 ± 0.21	2.57 ± 0.61	2.62 ± 0.20	2.69 ± 0.18		
[1.1, 1.6]	30	2.77 ± 0.29	2.58 ± 1.33	2.68 ± 0.33	2.88 ± 0.44	24	2.54 ± 0.47	4.45 ± 0.75	2.77 ± 0.41	2.83 ± 0.36		
$10.5 < M_*/M_\odot < 10^{11}$												
[0.7, 0.9]	94	3.43 ± 0.25	2.69 ± 0.52	3.20 ± 0.22	3.10 ± 0.21	83	2.77 ± 0.24	3.34 ± 0.68	2.92 ± 0.17	3.14 ± 0.23		
[0.9, 1.1]	73	3.58 ± 0.30	2.58 ± 0.48	3.28 ± 0.26	3.00 ± 0.24	93	2.70 ± 0.17	2.59 ± 0.47	2.68 ± 0.14	2.66 ± 0.16		
[1.1, 1.6]	63	3.20 ± 0.34	2.33 ± 0.46	2.93 ± 0.27	2.78 ± 0.23	101	2.07 ± 0.19	2.81 ± 0.55	2.24 ± 0.13	2.45 ± 0.20		
$R < 0.5 \times R_{200}$												
[0.7, 0.9]	56	3.18 ± 0.25	2.64 ± 0.63	3.03 ± 0.23	3.08 ± 0.19	123	2.76 ± 0.18	2.99 ± 0.51	2.84 ± 0.12	3.00 ± 0.12		
[0.9, 1.1]	69	3.33 ± 0.25	2.47 ± 0.43	3.09 ± 0.21	2.93 ± 0.19	135	2.70 ± 0.14	2.58 ± 0.29	2.65 ± 0.11	2.66 ± 0.12		
[1.1, 1.6]	61	2.98 ± 0.24	2.21 ± 0.65	2.75 ± 0.22	2.75 ± 0.27	125	2.10 ± 0.15	2.98 ± 0.51	2.29 ± 0.13	2.46 ± 0.19		
$R > 0.5 \times R_{200}$												
[0.7, 0.9]	74	3.91 ± 0.29	2.20 ± 0.99	3.44 ± 0.26	3.27 ± 0.40	123	2.76 ± 0.18	2.99 ± 0.54	2.83 ± 0.12	3.00 ± 0.12		
[0.9, 1.1]	27	3.86 ± 0.59	2.25 ± 1.60	3.54 ± 0.60	3.14 ± 0.55	135	2.70 ± 0.14	2.58 ± 0.31	2.65 ± 0.12	2.66 ± 0.12		
[1.1, 1.6]	32	3.24 ± 0.62	2.70 ± 1.18	3.04 ± 0.49	2.88 ± 0.37	125	2.10 ± 0.15	2.98 ± 0.51	2.29 ± 0.13	2.46 ± 0.19		
Without CANDELS data												
[0.7, 0.9]	130	3.56 ± 0.21	2.52 ± 0.59	3.23 ± 0.17	3.10 ± 0.16	100	2.66 ± 0.15	2.87 ± 0.58	2.72 ± 0.12	2.95 ± 0.17		
[0.9, 1.1]	96	3.44 ± 0.23	2.61 ± 0.34	3.18 ± 0.19	3.00 ± 0.19	95	2.56 ± 0.14	2.54 ± 0.39	2.55 ± 0.12	2.61 ± 0.12		
[1.1, 1.6]	93	3.06 ± 0.23	2.40 ± 0.41	2.83 ± 0.19	2.79 ± 0.20	46	2.71 ± 0.24	3.53 ± 0.35	2.83 ± 0.21	2.68 ± 0.15		
Spec. members only												
[0.7, 0.9]	60	3.36 ± 0.30	2.37 ± 0.46	3.08 ± 0.25	3.06 ± 0.25	122	2.76 ± 0.17	2.99 ± 0.54	2.84 ± 0.12	3.00 ± 0.12		
[0.9, 1.1]	32	3.21 ± 0.43	2.58 ± 1.09	2.99 ± 0.38	2.93 ± 0.28	129	2.69 ± 0.15	2.62 ± 0.36	2.67 ± 0.11	2.69 ± 0.12		
[1.1, 1.6]	62	3.05 ± 0.26	2.41 ± 0.63	2.85 ± 0.21	2.84 ± 0.26	83	2.32 ± 0.27	3.01 ± 0.46	2.50 ± 0.22	2.69 ± 0.16		

in Tables 10 and 11) are consistent so we would have not found the same results when considering a symmetric Gaussian fit. In fact, the difference is explained because the distribution of cluster galaxies is more skewed towards larger values of  $\gamma$  as seen in Fig. 12, e.g. cluster ETG show a population skewed towards larger galaxies with respect to the field which increases the mean. In particular, the skewness of the best model fit for cluster galaxies is clearly positive ( $s \sim 0.8$  for the three redshift bins) while the distribution of field galaxies present a negative skewness ( $-0.0$  to  $-0.4$ ). However, the differences in the median values are very moderate and even consistent with zero depending on the method used (see Table 10 and Fig. 14). As a sanity check, we overplot the size evolutions recently reported by Newman et al. (2012), Cimatti et al. (2012) and Damjanov et al. (2011) using independent data sets without environment distinction. Our results in the field are globally consistent with previous measurements by Newman et al. (2012) and Cimatti et al. (2012). The discrepancy is slightly larger ( $\sim 2\sigma$ ) with Damjanov et al. (2011) who measure  $\gamma \propto (1+z)^{-1.62 \pm 0.34}$  and a larger zero-point. We also show in Fig. 13 the sizes of ETGs in groups and in the field from Huertas-Company et al. (2013b), which also globally lie on the same relation. The points at  $z \sim 0$  are computed from the SDSS by cross-correlating the group catalogue of Yang et al. (2007) updated to the DR7 and the morphological classification of Huertas-Company et al. (2011). We select ETGs in the same stellar mass range ( $M_* > 3 \times 10^{10}$ ) than the high-redshift sample and compute  $\langle \gamma \rangle$  with the same methodology. We select as cluster galaxies

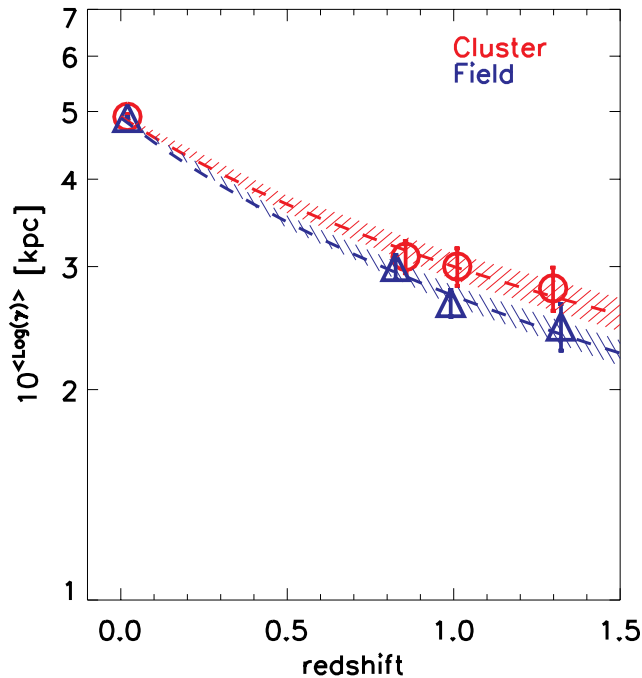
those living in the most massive haloes ( $M_h/M_\odot > 10^{14}$ ) and field galaxies are selected in the low-mass end of the halo mass function, i.e.  $M_h/M_\odot < 10^{13}$  (see Huertas-Company et al. 2013b for more details).

Since the difference between cluster and field galaxies is not seen in the local universe, field ETGs follow  $\gamma \propto (1+z)^\alpha$  with  $\alpha = -0.92 \pm 0.04$  and cluster ETGs have a value of  $\alpha = -0.53 \pm 0.04$  (see Table 12). The evolutions are therefore different at more than  $3\sigma$  when considering the average sizes.

The result is robust to morphological classifications. If we consider cluster and field ETGs visually classified, the small differences in the morphological classifications reported in Table 4 and Section 2.5 do not change the trends on the size evolution, i.e. the  $\alpha$  values from the best fits remain the same within the error bars. Also, when we consider only spectroscopically confirmed members, the result remains unchanged (Fig. 15). Finally, since the COSMOS sample is shallower than the other samples (see Section 3), incompleteness might have an impact in the size evolution. We have thus checked that our results do not change when the COSMOS sample is removed, even if our uncertainties become larger due to lower statistics. Another possible problem might come from the fact that in the last redshift bin, the field sample is dominated by optical rest-frame data (i.e. CANDELS) while the cluster sample is close to the UV rest-frame (ACS). As shown in Section 2.3, the  $\sim 20$  per cent difference between sizes estimated in the NIR and optical might enhance the difference. We have therefore checked the stability of

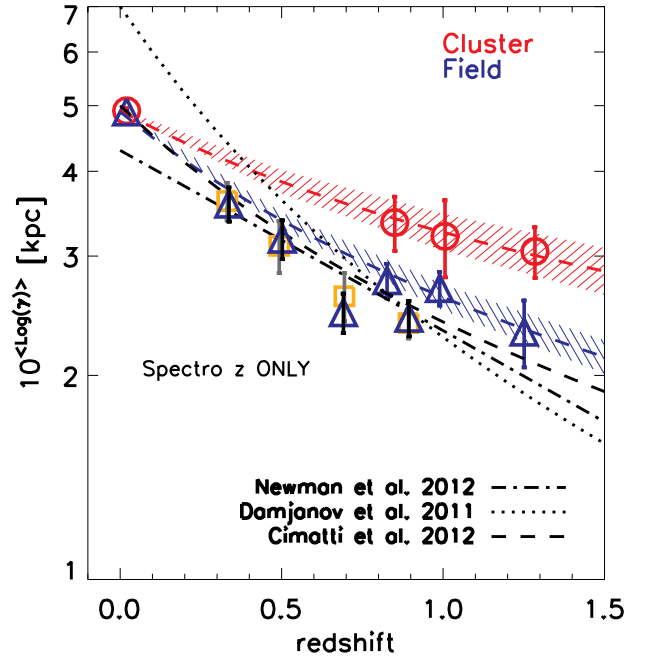
**Table 11.** Relative difference  $(10^{(\log \gamma)_{\text{cluster}}} - 10^{(\log \gamma)_{\text{field}}})/10^{(\log \gamma)_{\text{field}}}$  for four different ways of computing the characteristic size.

Redshift bin	All Q-ETGs			
	$\Delta_{\text{mean}}$	$\Delta_{\text{mode}}$	$\Delta_{\text{median}}$	$\Delta_{\text{median(notit)}}$
[0.7, 0.9]	$0.29 \pm 0.11$	$-0.16 \pm 0.24$	$0.14 \pm 0.07$	$0.03 \pm 0.07$
[0.9, 1.1]	$0.28 \pm 0.10$	$0.01 \pm 0.17$	$0.20 \pm 0.08$	$0.13 \pm 0.08$
[1.1, 1.6]	$0.46 \pm 0.12$	$-0.19 \pm 0.19$	$0.25 \pm 0.09$	$0.13 \pm 0.11$
$M_*/M_{\odot} > 10^{11}$				
[0.7, 0.9]	$0.24 \pm 0.14$	$-0.32 \pm 0.60$	$0.14 \pm 0.17$	$0.07 \pm 0.16$
[0.9, 1.1]	$0.16 \pm 0.16$	$-0.16 \pm 0.49$	$0.07 \pm 0.16$	$0.01 \pm 0.16$
[1.1, 1.6]	$0.09 \pm 0.21$	$-0.42 \pm 0.36$	$-0.02 \pm 0.19$	$0.02 \pm 0.20$
$M_*/M_{\odot} < 10^{11}$				
[0.7, 0.9]	$0.24 \pm 0.13$	$-0.19 \pm 0.25$	$0.09 \pm 0.09$	$-0.01 \pm 0.10$
[0.9, 1.1]	$0.33 \pm 0.13$	$-0.00 \pm 0.26$	$0.23 \pm 0.11$	$0.13 \pm 0.11$
[1.1, 1.6]	$0.55 \pm 0.20$	$-0.17 \pm 0.25$	$0.31 \pm 0.14$	$0.14 \pm 0.13$
$R < 0.5 \times R_{200}$				
[0.7, 0.9]	$0.15 \pm 0.11$	$-0.12 \pm 0.28$	$0.07 \pm 0.09$	$0.03 \pm 0.08$
[0.9, 1.1]	$0.24 \pm 0.10$	$-0.05 \pm 0.21$	$0.17 \pm 0.09$	$0.10 \pm 0.09$
[1.1, 1.6]	$0.42 \pm 0.14$	$-0.26 \pm 0.26$	$0.20 \pm 0.11$	$0.12 \pm 0.13$
$R > 0.5 \times R_{200}$				
[0.7, 0.9]	$0.42 \pm 0.13$	$-0.27 \pm 0.38$	$0.21 \pm 0.10$	$0.09 \pm 0.14$
[0.9, 1.1]	$0.43 \pm 0.23$	$-0.13 \pm 0.63$	$0.34 \pm 0.23$	$0.18 \pm 0.21$
[1.1, 1.6]	$0.54 \pm 0.31$	$-0.09 \pm 0.43$	$0.33 \pm 0.22$	$0.17 \pm 0.17$
Without CANDELS data				
[0.7, 0.9]	$0.34 \pm 0.10$	$-0.12 \pm 0.29$	$0.19 \pm 0.08$	$0.05 \pm 0.08$
[0.9, 1.1]	$0.35 \pm 0.11$	$0.03 \pm 0.20$	$0.25 \pm 0.09$	$0.15 \pm 0.08$
[1.1, 1.6]	$0.13 \pm 0.12$	$-0.32 \pm 0.16$	$-0.00 \pm 0.10$	$0.04 \pm 0.09$
Spec. members only				
[0.7, 0.9]	$0.22 \pm 0.13$	$-0.21 \pm 0.24$	$0.08 \pm 0.10$	$0.02 \pm 0.09$
[0.9, 1.1]	$0.19 \pm 0.17$	$-0.01 \pm 0.44$	$0.12 \pm 0.15$	$0.09 \pm 0.11$
[1.1, 1.6]	$0.31 \pm 0.16$	$-0.20 \pm 0.26$	$0.14 \pm 0.12$	$0.06 \pm 0.12$


**Figure 14.** Evolution of the median values of  $\log(\gamma)$  for passive ETGs with  $\log(M/M_{\odot}) \geq 10.5$  in clusters (red circles) and in the field (blue triangles). The points at  $z = 0$  show the value of  $\langle \gamma \rangle$  in the local universe in clusters and in the field respectively (see the text for details). Blue and red dashed lines show the best-fitting model  $\gamma \propto (1+z)^{\alpha}$  for field and cluster galaxies, respectively.

**Table 12.** Fit parameters of the size evolution of cluster and field ETGs as  $\gamma = \beta \times (1+z)^{\alpha}$ .

Sample	Mass	$\alpha \pm \Delta\alpha$	$\beta \pm \Delta\beta$
Cluster ETGs	$\log(M/M_{\odot}) \geq 10.5$	$-0.53 \pm 0.04$	$4.91 \pm 0.04$
Field ETGs	$\log(M/M_{\odot}) \geq 10.5$	$-0.92 \pm 0.04$	$4.89 \pm 0.02$


**Figure 15.** Same as Fig. 13 but only spectroscopically confirmed members are included in the cluster sample.

our results if the CANDELS data are not included in the analysis (see Table 10). As expected, the effect is mostly seen in the highest redshift bin where we expect a stronger impact of band shifting in the size determination. The mean size difference at  $z > 1$  is in fact not significant ( $0.13 \pm 0.12$ ) when the CANDELS data are removed. This might be due either to the difference in rest-frame bandpass or also a consequence of incompleteness and low SNR of the field sample, since COSMOS data alone start to be affected by incompleteness at these redshifts as discussed in Section 3.

## 5 DISCUSSION

Massive ETGs living in massive clusters ( $M/M_{\odot} > 10^{14}$ ) at  $0.8 < z < 1.5$  appear to be on average 1.5 times larger than galaxies of the same stellar mass residing in the field. While the peak of the size distribution in different environments is similar, clusters show a tail of larger galaxies at higher redshifts. Similar results have been obtained by Papovich et al. (2012) on a single cluster at  $z \sim 1.6$  but no significant difference was measured by Raichoor et al. (2012) in the Lynx supercluster at  $z \sim 1.3$ .

Interestingly, this size difference is not seen in the nearby Universe (Huertas-Company et al. 2013a, Poggianti et al. 2013) where cluster and field galaxies present similar sizes. If cluster galaxies are growing faster at earlier epochs, then this growth must slow related to the fields, as galaxies in both environments end up with

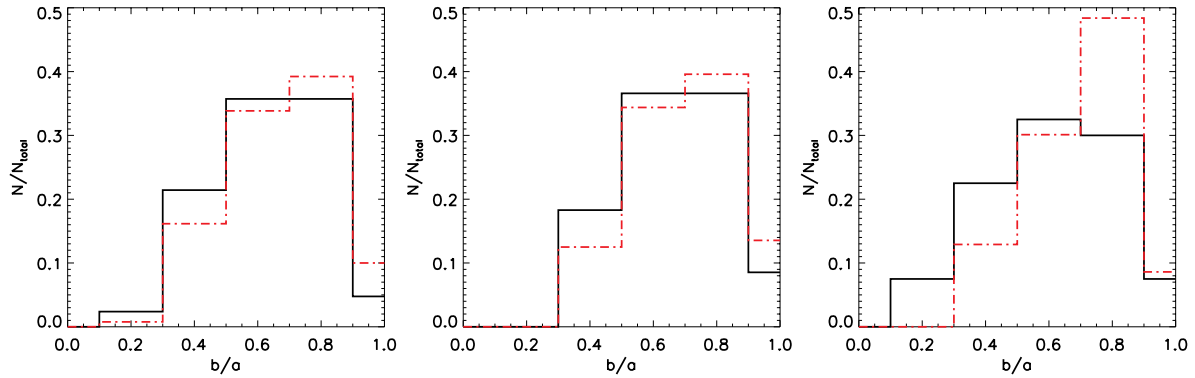


**Figure 16.** Axis ratio distributions for field (black solid lines) and cluster (red dashed lines) in the three redshift bins considered in this work. Cluster galaxies appear on average rounder than field galaxies.

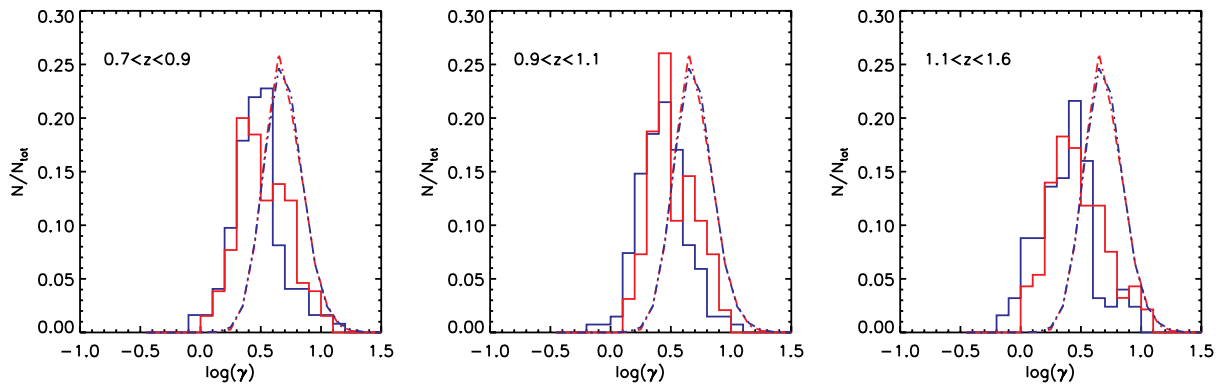


**Figure 17.** Distributions of  $\log(\gamma)$  in three different redshift bins as labelled, for cluster and field galaxies in our sample (red and blue solid lines, respectively) as compared to the distribution of galaxies at  $z \sim 0$  from the SDSS in clusters and in the field (dash-dotted red and blue lines, respectively).

the same size distribution by zero redshift. In Fig. 17, we compare the distributions of  $\log(\gamma)$  in the three redshift bins probed by our sample with the same distribution in the SDSS.

Clearly, the local distributions for cluster and field galaxies are undistinguishable, peak at larger sizes and are symmetric (e.g. Huertas-Company et al. 2013b). The smallest galaxies have disappeared in the low-redshift sample. The small end of the high-redshift distribution gradually fills up the peak of the local: there is a transition of the peak of the galaxy distribution from smaller to larger sizes. During this transition phase, the high-redshift size distributions are skewed towards larger values and, according to our data, this process has already started in clusters at  $z \sim 1$ , while it is not yet observed in the field.

If at least part of the evolution seen in  $\gamma$  is due to mergers, the difference, we see between cluster and field galaxies might reflect the fact that on average cluster galaxies at  $z \sim 1$  have experienced more mergers than field galaxies at the same epoch, probably during the formation phase of the clusters when velocity dispersions are lower. Since the size evolution from  $z \sim 1$  to present is then slower in clusters than in the field (as shown in Section 4.4), the mechanism that increased sizes of cluster galaxies should drop its efficiency, e.g. cluster galaxy merger rates become lower than in the field due probably to the increase of the galaxy velocity dispersion. If this is true, we should observe that these larger galaxies in high-redshift clusters are concentrated in their cores, where in these early epochs dynamical friction and higher densities cause a higher merger rate with respect to their outskirts. Fig. 18 shows the size evolution for

galaxies residing in the cluster core ( $R < 0.5 \times R_{200}$ ) as compared to those living in the outskirts ( $R < 0.5 \times R_{200}$ ) showing no significant difference.

To better understand which galaxies are increasing their sizes in clusters, in Fig. 19 we split our sample in two bins of stellar mass ( $10.5 < \log(M_*/M_\odot) < 11$  and  $\log(M_*/M_\odot) > 11$ ). This threshold is selected since  $10^{11} M_*/M_\odot$  appears to be a critical mass above which galaxy evolution is expected to be dominated by mergers (e.g. De Lucia et al. 2006; Khochfar & Silk 2011; Shankar et al., in preparation, and references therein) so we might naturally expect that the behaviour against environment could differ for these two populations. Interestingly, we find that for the most massive galaxies ( $M_*/M_\odot > 10^{11}$ ) the difference is somehow less pronounced. This might be evidence that very massive galaxies in both environments have experienced similar size growth, even though we have lower statistics in that bin to establish a clear conclusion.

Galaxies with mass  $10.5 < \log(M_*/M_\odot) < 11$  show larger sizes in clusters. In this mass range, mergers should not be as efficient as for galaxies of higher masses. However, the environmental differences that we observe are driven by these masses, suggesting that other mechanisms might contribute to the size enlargement. In fact, an important point is that the evolution of  $\gamma$  does not measure the individual evolution of galaxies. As several works have pointed out (e.g. van der Wel et al. 2009; Newman et al. 2012; Carollo et al. 2013), the evolution we see could be partially or even dominated by the quenching and morphological transformations of new larger

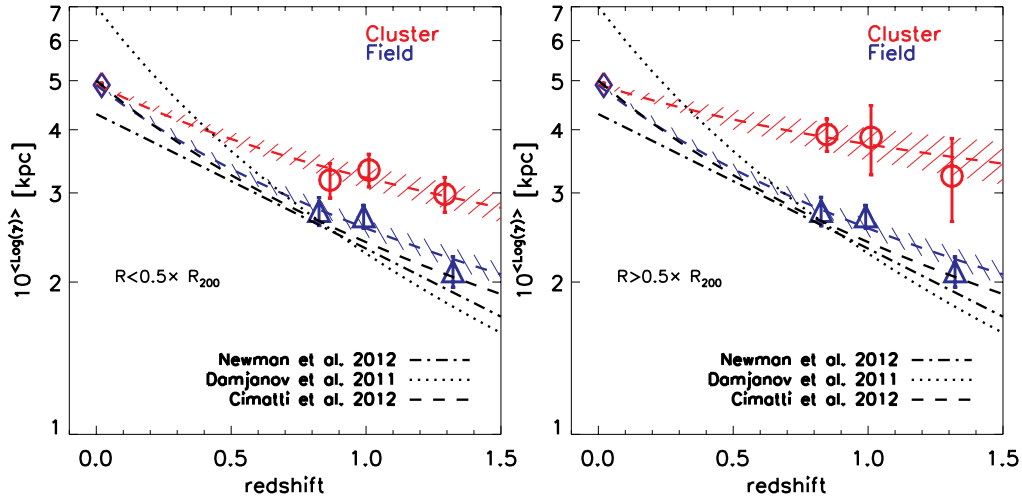


**Figure 18.** Redshift evolution of  $\gamma$  in clusters (red circles) and in the field (blue triangles) for galaxies living in the central parts of the cluster ( $R < 0.5 \times R_{200}$ , left-hand panel) and in the outskirts ( $R > 0.5 \times R_{200}$ , right-hand panel) as labelled. Symbols are the same than for Fig. 13.

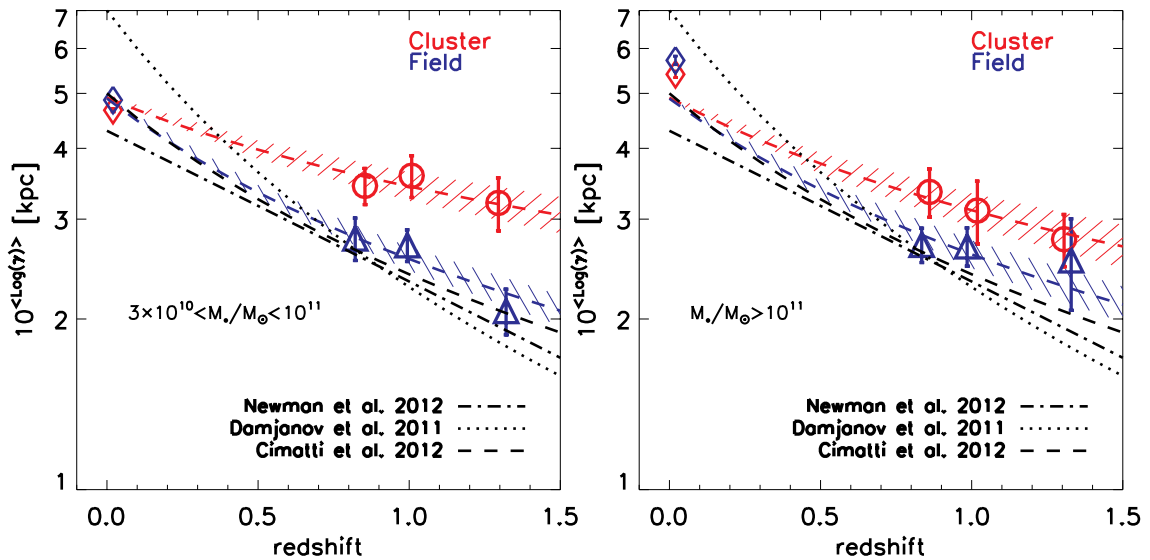


**Figure 19.** Redshift evolution of  $\gamma$  in clusters (red circles) and in the field (blue triangles) for galaxies in the stellar mass range  $3 \times 10^{10} < M_*/M_\odot < 10^{11}$  (left-hand panel) and  $M_*/M_\odot > 10^{11}$  (right-hand panel). Symbols are the same than for Fig. 13.

galaxies which enter the mass selection at later epochs. In this case, our results would reflect the fact the quenching is more efficient in the cluster environment, so it happens at earlier epochs. This would explain also why the environmental size differences are larger in the lower mass bin, since they are quenched later than more massive galaxies and more efficiently in clusters (e.g. Thomas et al. 2005).

Another possibility is a different morphological mixing in clusters and in the field. Huertas-Company et al. (2013b) and Bernardi et al. (2012) have shown that lenticular galaxies, which on average have lower axis ratios, are also more compact when the circularized size is used (see also Newman et al. 2013). Therefore, at first level, a different axis ratio distribution in the two environments could result in apparent size differences. Fig. 19 shows the  $b/a$  distributions for field and cluster galaxies in the three redshift bins. The distributions are only clearly statistically different for the highest redshift bin ( $P_{KS} \sim 0.02$  for  $z > 1.1$  and  $P_{KS} \sim 0.2$  for  $z < 1.1$ ) but the median

values of  $b/a$  are systematically larger for cluster galaxies at all redshifts (see Table 13).

It is unclear how and why we reach a perfect match between the size distributions in the two environments at  $z \sim 0$ , and what happens at  $z < 1$ . Huertas-Company et al. (2013b) have shown that in the COSMOS field, there are not significant differences in the MSR and size evolution of galaxies in groups and in the field. However, for a DEEP2 field spectroscopic sample, Cooper et al.

**Table 13.** Median values of  $b/a$  for cluster and field ETGs with  $\log(M_*/M_\odot)$  in three redshift bins.

	Cluster	Field
$0.7 < z < 0.9$	$0.69 \pm 0.01$	$0.64 \pm 0.02$
$0.9 < z < 1.1$	$0.72 \pm 0.01$	$0.66 \pm 0.02$
$1.1 < z < 1.6$	$0.73 \pm 0.01$	$0.62 \pm 0.03$

(2012) found that larger galaxies with high Sérsic index ( $n > 2.5$ ) preferentially live in dense environments (defined as the number of neighbours).

## 6 SUMMARY AND CONCLUSIONS

We have studied the MSRs as well as the size evolution of 319 passive ETGs with  $\log(M/M_{\odot}) > 10.5$  living in nine well-known rich clusters between  $z = 0.8$  and  $z \sim 1.5$ . The sample is 80 per cent complete for objects with  $\log(M_*/M_{\odot}) > 10.5$ . This is the largest sample of cluster galaxies at those redshifts used for this kind of study. The results are compared with the ones obtained on a sample of 382 field ETGs in the same mass and redshift range.

Our main results are summarized in the following:

(i) When no selection in star formation or morphology is performed, we find that the fraction of SDGs, defined as those galaxies with  $\Sigma_{50} > 3 \times 10^9 M_{\odot} \text{ kpc}^{-2}$  and  $10.5 < \log(M/M_{\odot}) < 11.6$  is slightly larger in the clusters than in the field ( $32_{-3}^{+4}$  per cent versus  $21_{-3}^{+4}$  per cent). Around,  $\sim 70$  per cent of the SDGs have a disc component.

If passive ETGs are selected, then

(ii) The slopes of the MSRs of ETGs in clusters do not change significantly up to  $z \sim 1.2$  being the typical value  $\beta = 0.49 \pm 0.08$  which is also consistent with previous works at lower redshifts without environment distinction. Our results are in favour of a very mild evolution of the slope of the MSR of ETGs from  $z \sim 1.2$  independently of the environment. For the three clusters at  $z > 1.2$ , we measure  $\beta = 0.27 \pm 0.06$ , which might indicate a lack of massive and large ETGs at these higher redshifts.

(iii) The zero-point of the MSR changes with time. Cluster ETGs with  $\log(M_*/M_{\odot}) > 10.5$  roughly doubled their median size from  $z \sim 1.5$ . Our results are in agreement with previous published results without environment distinction.

(iv) We parametrize the size using the mass-normalized size,  $\gamma = R_e/M_{11}^{0.57}$ . The  $\gamma$  distributions in clusters and in the field peak at the same position but the distributions in clusters are more skewed towards larger sizes. This results on average mass normalized sizes  $\sim 30 \pm 10$  per cent times larger in clusters than in the field. The difference is however not significant when the median sizes are considered ( $\sim 10 \pm 10$  per cent).

(v) In our sample, the difference is driven by low mass ( $10.5 < \log(M_*/M_{\odot}) < 11$ ) galaxies independently of their location in the cluster up to  $R_{200}$ .

(vi) Because the difference is most pronounced for low-mass galaxies, it would be better explained by accelerated quenching and/or different morphological mixings rather than by a higher merger activity in the cluster environment at higher redshift. Cluster galaxies appear on average rounder than field galaxies at fixed stellar mass.

(vii) The size difference seen at high redshift is not observed in the local universe. Cluster galaxies show therefore a less steep evolution with evolution coefficients  $-0.53 \pm 0.04$ , and  $-0.92 \pm 0.04$  for clusters and field, respectively. For median sizes, we do not measure this difference, and obtain  $-0.84 \pm 0.04$  in the field and  $-0.71 \pm 0.05$  in clusters.

## ACKNOWLEDGEMENTS

The authors would like to thank G. Rousset for pointing out interesting suggestions and E. Daddi, V. Strazzulo, R. Gobat for stimulating discussions. RD gratefully acknowledges the support provided by

the BASAL Center for Astrophysics and Associated Technologies (CATA), and by FONDECYT grant no. 1130528.

## REFERENCES

- Andreon S., Valtchanov I., Jones L. R., Altieri B., Bremer M., Willis J., Pierre M., Quintana H., 2005, *MNRAS*, 359, 1250
- Arnouts S., Cristiani S., Moscardini L., Matarrese S., Lucchin F., Fontana A., Giallongo E., 1999, *MNRAS*, 310, 540
- Barden M. et al., 2005, *ApJ*, 635
- Bassett R. et al., 2013, *ApJ*, 770, 58
- Benítez N. et al., 2004, *ApJS*, 150, 1
- Bernardi M., 2009, *MNRAS*, 395, 1491
- Bernardi M., Shankar F., Hyde J. B., Mei S., Marulli F., Sheth R. K., 2010, *MNRAS*, 404, 2087
- Bernardi M., Meert A., Vikram V., Huertas-Company M., Mei S., Shankar F., Sheth R. K., 2012, preprint ([arXiv:e-prints](https://arxiv.org/abs/1205.3443))
- Bertin E., Arnouts S., 1996, *A&AS*, 117, 393
- Bezanson R., van Dokkum P. G., Tal T., Marchesini D., Kriek M., Franx M., Coppi P., 2009, *ApJ*, 697, 1290
- Bluck A. F. L., Conselice C. J., Bouwens R. J., Daddi E., Dickinson M., Papovich C., Yan H., 2009, *MNRAS*, 394, L51
- Böhringer H. et al., 2007, *A&A*, 469, 363
- Brammer G. B., van Dokkum P. G., Coppi P., 2008, *ApJ*, 686, 1503
- Bremer M. N. et al., 2006, *MNRAS*, 371, 1427
- Bruzual G., Charlot S., 2003, *MNRAS*, 344, 1000 (BC03)
- Buitrago F., Trujillo I., Conselice C. J., Bouwens R. J., Dickinson M., Yan H., 2008, *ApJ*, 687, L61
- Bundy K. et al., 2006, *ApJ*, 651, 120
- Bundy K. et al., 2010, *ApJ*, 719, 1969
- Cappellari M., 2013, *ApJ*, 778, L2
- Carollo C. M. et al., 2013, *ApJ*, 773, 112
- Casali M. et al., 2006, in McLean I. S., Iye M., eds, *Proc. SPIE Conf. Ser.*, Vol. 6269, *Ground-based and Airborne Instrumentation for Astronomy*. SPIE, Bellingham, p. 62690W
- Cassata P. et al., 2011, *ApJ*, 743, 96
- Chabrier G., 2003, *ApJ*, 586, L133
- Cimatti A., Nipoti C., Cassata P., 2012, *MNRAS*, 422, L62
- Cooper M. C. et al., 2012, *MNRAS*, 419, 3018
- Daddi E. et al., 2005, *ApJ*, 626, 680
- Damjanov I. et al., 2011, *ApJ*, 739, L44
- Dawson K. S. et al., 2009, *ApJ*, 138
- De Lucia G., Springel V., White S. D. M., Croton D., Kauffmann G., 2006, *MNRAS*, 366, 499
- Della Ceca R., Scaramella R., Gioia I. M., Rosati P., Fiore F., Squires G., 2000, *A&A*, 353, 498
- Demarco R. et al., 2005, *A&A*, 432, 381
- Demarco R. et al., 2007, *ApJ*, 663, 164
- Demarco R. et al., 2010, *ApJ*, 725, 1252
- Díaz-García L. A., Mármol-Queraltó E., Trujillo I., Cenarro A. J., López-Sanjuan C., Pérez-González P. G., Barro G., 2013, *MNRAS*, 433, 60
- Duc P.-A. et al., 2011, *MNRAS*, 417, 863
- Ettori S., Morandi A., Tozzi P., Balestra I., Borgani S., Rosati P., Lovisari L., Terenzi F., 2009, *A&A*, 501, 61
- Faloon A. J. et al., 2013, *ApJ*, 768, 104
- Fan L., Lapi A., De Zotti G., Danese L., 2008, *ApJ*, 689, L101
- Fan L., Lapi A., Bressan A., Bernardi M., De Zotti G., Danese L., 2010, *ApJ*, 718, 1460
- Fassbender R., Böhringer H., Santos J., Lamer G., Mullis C., Schuecker P., Schwobe A., Rosati P., 2007, in Aschenbach B., Burwitz V., Hasinger G., Leibundgut B., eds, *Relativistic Astrophysics Legacy and Cosmology - Einstein's Legacy*. Springer-Verlag, Berlin, p. 307
- Fernández-Lorenzo M., Sulentic J., Verdes-Montenegro L., Argudo-Fernández M., 2013, *MNRAS*, 434, 325
- Ford H., 2004, HST Proposal ID 10327, ACS Imaging of a High-Redshift Cluster of Galaxies
- George M. R. et al., 2011, *ApJ*, 742, 125

- Giavalisco M. et al., 2004, *ApJ*, 600, L93
- Gilbank D. G., Yee H. K. C., Ellingson E., Hicks A. K., Gladders M. D., Barrientos L. F., Keeney B., 2008, *ApJ*, 677, L89
- Gilbank D. G., Gladders M. D., Yee H. K. C., Hsieh B. C., 2011, *ApJ*, 141, 94
- Gladders M. D., Yee H. K. C., 2005, *VizieR Online Data Catalog*, 215, 70001
- Grogin N. A. et al., 2011, *ApJS*, 197, 35
- Guo Q., White S., Li C., Boylan-Kolchin M., 2010, *MNRAS*, 404, 1111
- Gutiérrez C. M., Trujillo I., Aguerri J. A. L., Graham A. W., Caon N., 2004, *ApJ*, 602, 664
- Hicks A. K. et al., 2008, *ApJ*, 680, 1022
- Hilton M. et al., 2009, *ApJ*, 697, 436
- Hilton M. et al., 2010, *ApJ*, 718, 133
- Hopkins P. F., Bundy K., Murray N., Quataert E., Lauer T. R., Ma C.-P., 2009, *MNRAS*, 398, 898
- Huertas-Company M., Rouan D., Tasca L., Soucail G., Le Fèvre O., 2008, *A&A*, 478, 971
- Huertas-Company M., Foex G., Soucail G., Pelló R., 2009, *A&A*, 505, 83
- Huertas-Company M., Aguerri J. A. L., Bernardi M., Mei S., Sánchez Almeida J., 2011, *A&A*, 525, A157
- Huertas-Company M., Shankar F., Mei S., Bernardi M., Aguerri J. A. L., Meert A., Vikram V., 2013a, *ApJ*, 779, 29
- Huertas-Company M. et al., 2013b, *MNRAS*, 428, 1715
- Ilbert O. et al., 2006, *A&A*, 457, 841
- Ilbert O. et al., 2010, *ApJ*, 709, 644
- Jee M. J. et al., 2011, *ApJ*, 737, 59
- Khochfar S., Silk J., 2011, *MNRAS*, 410, L42
- Koekemoer A. M. et al., 2011, *ApJS*, 197, 36
- Krist J. E., Hook R. N., Stoehr F., 2011, in Kahan M. A., ed., *SPIE Conf. Ser.*, Vol. 8127, *Optical Modeling and Performance Predictions*. SPIE, Bellingham, p. 81270J
- Larson R. B., 1975, *MNRAS*, 173, 671
- Lidman C., Rosati P., Demarco R., Nonino M., Mainieri V., Stanford S. A., Toft S., 2004, *A&A*, 416, 829
- Lidman C. et al., 2013, *MNRAS*, 433, 825
- López-Sanjuan C., Balcells M., Pérez-González P. G., Barro G., García-Dabó C. E., Gallego J., Zamorano J., 2009, *A&A*, 501, 505
- López-Sanjuan C., Balcells M., Pérez-González P. G., Barro G., Gallego J., Zamorano J., 2010, *A&A*, 518, A20
- López-Sanjuan C. et al., 2012, *A&A*, 548, A7
- Maltby D. T., 2010, *MNRAS*, 402, 282
- Martinez-Manso J. et al., 2011, *ApJ*, 738, L22
- Mei S. et al., 2009, *ApJ*, 690, 42
- Mei S. et al., 2012, *ApJ*, 754, 141
- Meyers J. et al., 2010, *BAAS*, 42, 492
- Meyers J. et al., 2012, *ApJ*, 750, 1
- Moorwood A., Cuby J.-G., Lidman C., 1998a, *The Messenger*, 91, 9
- Moorwood A. et al., 1998b, *The Messenger*, 94, 7
- Naab T., Johansson P. H., Ostriker J. P., 2009, *ApJ*, 699, L178
- Nair P. B., Abraham R. G., 2010, *ApJS*, 186, 427
- Newman A. B., Ellis R. S., Treu T., Bundy K., 2010, *ApJ*, 717, L103
- Newman A. B., Ellis R. S., Bundy K., Treu T., 2012, *ApJ*, 746, 162
- Newman A. B., Ellis R. S., Andreon S., Treu T., Raichoor A., Trinchieri G., 2013, preprint ([arXiv:1310.6754](https://arxiv.org/abs/1310.6754))
- Oke J. B., Gunn J. E., 1983, *ApJ*, 226, 713
- Papovich C. et al., 2010, *ApJ*, 716, 1503
- Papovich C. et al., 2012, *ApJ*, 750, 93
- Partridge R. B., Peebles P. J. E., 1967, *ApJ*, 147, 868
- Pelló R. et al., 2009, *A&A*, 508, 1173
- Peng C. Y., Ho L. C., Impey C. D., Rix H., 2002, *AJ*, 124, 266
- Pierre M. et al., 2004, *J. Cosmol. Astropart. Phys.*, 9, 11
- Pirard J.-F. et al., 2004, in Moorwood A. F. M., Iye M., eds, *Proc. SPIE Conf. Ser.*, Vol. 5492, *Ground-Based Instrumentation for Astronomy*. SPIE, Bellingham, p. 1763
- Poggianti B. et al., 2013, *ApJ*, 762, 77
- Postman M. et al., 2005, *ApJ*, 623, 721
- Pović M. et al., 2013, *MNRAS*, 435, 3444
- Pozzetti L. et al., 2010, *A&A*, 523, A13
- Press W. H., Teukolsky S. A., Vetterling W. T., Flannery B. P., 1992, *Numerical Recipes in C. The Art of Scientific Computing*. Cambridge Univ. Press, Cambridge
- Ragone-Figueroa C., Granato G. L., 2011, *MNRAS*, 414, 3690
- Raichoor A. et al., 2011, *ApJ*, 732, 12
- Raichoor A. et al., 2012, *ApJ*, 745, 130
- Rettura A. et al., 2010, *ApJ*, 709, 512
- Rosati P., della Ceca R., Norman C., Giacconi R., 1998, *ApJ*, 492, L21
- Rosati P. et al., 2004, *AJ*, 127, 230
- Rosati P. et al., 2009, *A&A*, 508, 583
- Santini P. et al., 2009, *A&A*, 504, 751
- Santos J. S. et al., 2009, *A&A*, 501, 49
- Saracco P., Longhetti M., Gargiulo A., 2011, *MNRAS*, 412, 2707
- Scodreggio M., 2001, *AJ*, 121, 2413
- Scoville N. et al., 2007, *ApJS*, 172, 1
- Sersic J. L., 1968, *Atlas de galaxias australes*. Observatorio Astronomico, Cordoba
- Shankar F., Marulli F., Bernardi M., Boylan-Kolchin M., Dai X., Khochfar S., 2010, *MNRAS*, 405, 948
- Sirianni M. et al., 2005, *PASP*, 117, 1049
- Stanford S. A. et al., 2006, *ApJ*, 646
- Strazzullo V. et al., 2010, *A&A*, 524, A17
- Szomoru D., Franx M., van Dokkum P. G., Trenti M., Illingworth G. D., Labbé I., Oesch P., 2013, *ApJ*, 763, 73
- Tanaka M., Finoguenov A., Ueda Y., 2010, *ApJ*, 716, L152
- Thomas D., Maraston C., Bender R., Mendes de Oliveira C., 2005, *ApJ*, 621, 673
- Trujillo I. et al., 2006, *ApJ*, 650, 18
- Trujillo I., Carrasco E. R., Ferré-Mateu A., 2012, *ApJ*, 751, 45
- Valentinuzzi T. et al., 2010a, *ApJ*, 712, 226
- Valentinuzzi T. et al., 2010b, *ApJ*, 721, L19
- van de Sande J. et al., 2011, *ApJ*, 736, L9
- van der Wel A., Bell E. F., van den Bosch F. C., Gallazzi A., Rix H.-W., 2009, *ApJ*, 698, 1232
- van Dokkum P. G., Franx M., Kelson D. D., Illingworth G. D., Fisher D., Fabricant D., 1998, *ApJ*, 500, 714
- van Dokkum P. G., Franx M., Fabricant D., Illingworth G. D., Kelson D. D., 2000, *ApJ*, 541, 95
- van Dokkum P. G. et al., 2008, *ApJ*, 677, L5
- van Dokkum P. G. et al., 2010, *ApJ*, 709, 1018
- Weinmann S. M., Kauffmann G., van den Bosch F. C., Pasquali A., McIntosh D. H., Mo H., Yang X., Guo Y., 2009, *MNRAS*, 394, 1213
- White S. D. M. et al., 2005, *A&A*, 444, 365
- Yang X., Mo H. J., van den Bosch F. C., Pasquali A., Li C., Barden M., 2007, *ApJ*, 671, 153

## APPENDIX A: CLUSTER SAMPLE

(i) RX J0152–1357 (hereafter RX0152) at  $z = 0.84$  was discovered in the ROSAT Deep Cluster Survey (RDCS; Rosati et al. 1998; Della Ceca et al. 2000) as an extended double-core X-ray source. Demarco et al. (2005, 2010) confirmed spectroscopically 134 galaxies as cluster members. The velocity dispersion of the most massive of the central subclusters is  $\sigma \sim 920 \text{ km s}^{-1}$  (Demarco et al. 2005). Its virial mass derived from the X-ray measurement is  $M_{200} = 7.3^{+1.8}_{-1.7} \times 10^{14} M_{\odot}$  (Ettori et al. 2009) whereas its mass derived from weak-lensing analysis is  $M_{200} = 4.4^{+0.7}_{-0.5} \times 10^{14} M_{\odot}$  (Jee et al. 2011). This cluster was observed with ACS WFC in 2002 November, in the *F625W* ( $r_{625}$ ), *F775W* ( $i_{775}$ ) and *F850LP* ( $z_{850}$ ) bandpasses. The exposure time was of 19 000, 19 200 and 19 000 s, respectively. Our NIR image in the  $K_s$  band was acquired using HAWK-I (Pirard et al. 2004; Casali et al. 2006) on Yepun (UT4) on the Very Large Telescope (VLT) at the ESO Cerro Paranal Observatory in 2009 October and has a PSF width of 0.4 arcsec.

(ii) RCS 2319+0038 (hereafter RCS2319) at  $z = 0.91$ : the clusters with the RCS prefix were observed in the context of the Red sequence Cluster Survey (RCS; Gladders & Yee 2005). The virial mass derived from the X-ray measurements of Hicks et al. (2008) is  $M_{200} = 5.4_{-1.0}^{+1.2} \times 10^{14} M_{\odot}$ . RCS2319 was observed with ACS WFC in the  $i_{775}$  and  $z_{850}$  bandpasses in 2006 May with a total exposure time of 2400 and 6800 s, respectively. The NIR images were acquired in the  $J_s$  band using ISAAC on Melipal (VLT-UT3; Moorwood et al. 1998b) in 2003 July with an average PSF width of 0.63 arcsec (Muñoz et al. in preparation) and in the  $K_s$  band using HAWK-I in 2009 November, with a PSF width of 0.47 arcsec. We have 11 spectroscopic confirmed members (Gilbank et al. 2008, 2011; Meyers et al. 2010).

(iii) XMMU J1229+0151 (hereafter XMM1229) at  $z = 0.98$  was initially detected in the *XMM-Newton* Distant Cluster Project (Böhlinger et al. 2007; Fassbender et al. 2007). This cluster is a rich, hot and X-ray-luminous galaxy cluster (Santos et al. 2009). The mass measured with lensing is  $M_{200} = 5.3_{-1.2}^{+1.7} \times 10^{14} M_{\odot}$  (Jee et al. 2011) whereas the virial mass from X-ray measurements is  $M_{200} = 5.7_{-0.8}^{+1.0} \times 10^{14} M_{\odot}$  (Santos et al. 2009). 27 cluster members were spectroscopically confirmed with the VLT/FORS2 spectrograph (Santos et al. 2009). In the framework of the Supernova Cosmology Project (Dawson et al. 2009), we obtained ACS/WFC images in the  $i_{775}$  and the  $z_{850}$  bandpasses in 2005 December, for total exposures of 4110 and 10 940 s, respectively. NIR imaging in the  $J$  band was acquired using SOFI (Moorwood, Cuby & Lidman 1998a) at the New Technology Telescope at the ESO/La Silla observatory in 2007 March, whereas the  $K_s$ -band imaging was acquired using HAWK-I in 2010 January. The  $J$ -band data have a PSF width of 0.98 arcsec and the  $K$  band have a PSF width of 0.41 arcsec. This cluster was also observed in the  $F160W$  bandpass with the WFC3 on *HST* in 2010 May, with a PSF width of 0.3 arcsec, and a pixel scale of 0.1282 arcsec pixel<sup>-1</sup>.

(iv) RCS 0220–0333 (hereafter RCS0220) at  $z = 1.03$  is an optically rich cluster at  $z = 1.03$  with 14 spectroscopic confirmed members (Meyers et al. 2010; Gilbank et al. 2011). The weak-lensing mass of the cluster is  $M_{200} = 4.8_{1.3}^{+1.8} \times 10^{14} M_{\odot}$  with a predicted velocity dispersion of  $881_{-74}^{+68} \text{ km s}^{-1}$  (Jee et al. 2011). This cluster was observed with ACS/WFC in the  $i_{775}$  and  $z_{850}$  bandpasses in 2005 with a total exposure of 2955 and 14 420 s, respectively. The NIR images were acquired in the  $J_s$  band using ISAAC in 2002 October, with a PSF width of 0.47 arcsec and in the  $K_s$  band using HAWK-I in 2010 January, with a PSF width of 0.35 arcsec.

(v) RCS 2345–3633 at  $z = 1.04$ : RCS 2345–3633 is an optically rich cluster at  $z = 1.04$  with 23 spectroscopic confirmed cluster members (Meyers et al. 2010; Gilbank et al. 2011). The virial mass estimated by weak lensing in Jee et al. (2011) is  $M_{200} = 2.14_{-0.7}^{+1.1} \times 10^{14} M_{\odot}$ . As the previous one, this cluster was observed with ACS/WFC in the  $i_{775}$  and  $z_{850}$  bandpasses in 2006 July with a total exposure of 4450 and 9680 s, respectively. The NIR images were acquired in  $J_s$  band using ISAAC in 2003 July (Muñoz et al., in preparation) and in  $K_s$  band using HAWK-I in

2010 October. The PSF width for HAWK-I image is 0.39 arcsec and for ISAAC image, it is 0.56 arcsec.

(vi) XMMMLSS 0223–0436 (hereafter XMM0223) at  $z = 1.22$ : XMMMLSS 0223–0436 was discovered in the *XMM* Large Scale Survey (LSS; Pierre et al. 2004; Andreon et al. 2005). Jee et al. (2011) estimated that the virial mass of this cluster from weak-lensing analysis is  $M_{200} = 7.4_{-1.8}^{+2.5} \times 10^{14} M_{\odot}$ , more than two times larger than the virial mass from X-ray measurements (Bremer et al. 2006). We used optical images from ACS WFC in  $F775W$  and  $F850LP$  bandpasses acquired in 2005 September and July with a total exposure time of 3380 and 14 020 s, respectively. XMMMLSS 0223 has NIR imaging in the  $J_s$ - and  $K_s$  band obtained with HAWK-I in 2009 November. The NIR PSF width is of 0.40 arcsec in the  $J_s$  band and of 0.38 arcsec in the  $K_s$  band. 23 cluster members were spectroscopically confirmed (Bremer et al. 2006; Meyers et al. 2010).

(vii) RDCS J1252–2927 (hereafter RDCS1252) at  $z = 1.23$  was discovered in the RDCS (Rosati et al. 1998) and confirmed as a cluster at  $z = 1.23$  based on an extensive spectroscopic campaign using the VLT (Lidman et al. 2004; Rosati et al. 2004). The virial mass based on a lensing analysis on deeper ACS images is  $M_{200} = 6.8_{-1.0}^{+1.2} \times 10^{14} M_{\odot}$  (Jee et al. 2011) whereas X-ray measurements gives  $M_{200} = 7.6 \pm 1.2 \times 10^{14} M_{\odot}$  (Ettori et al. 2009). For this cluster, we have 38 spectroscopic confirmed members from Demarco et al. (2007). Imaging ACS WFC in the  $i_{775}$  and  $z_{850}$  bandpasses were acquired in 2002 May with exposure times of 29 945 and 57 070 s, respectively. NIR data were obtained from ISAAC in  $J_s$ - and  $K_s$  band with a PSF width of 0.51 and 0.42 arcsec respectively.

(viii) XMMU J2235–2557 (hereafter XMM2235) at  $z = 1.39$ : XMMU J2235–2557 is one of the most massive X-ray luminous cluster at  $z > 1$  with a virial mass  $M_{200} \sim 6 \times 10^{14} M_{\odot}$  derived by X-ray measurement (Rosati et al. 2009). The mass from weak-lensing analysis is  $M_{200} = 7.3_{-1.4}^{+1.7} \times 10^{14} M_{\odot}$  (Jee et al. 2011). Optical images were acquired using ACS WFC in the  $i_{775}$  and  $z_{850}$  bandpasses in 2005 June. The total exposure time are 8150 and 14 400 s, respectively. NIR imaging in  $J_s$ - and  $K_s$  band were taken using HAWK-I in 2007 October with a PSF width of 0.52 and 0.37 arcsec, respectively. 31 cluster members were spectroscopically confirmed (Rosati et al. 2009).

(ix) XMMXCS J2215–1738 (hereafter XMM2215) at  $z = 1.45$  was the highest redshift cluster spectroscopically confirmed (Stanford et al. 2006) until the recent discovery of CIG J0218–0510 at  $z = 1.62$  (Papovich et al. 2010; Tanaka, Finoguenov & Ueda 2010). The virial mass from X-ray measurement is  $M_{200} = 2.0_{-0.6}^{+0.5} \times 10^{14} M_{\odot}$  (Hilton et al. 2010) and the one derived from weak lensing is  $M_{200} = 4.3_{-1.7}^{+3.0} \times 10^{14} M_{\odot}$  (Jee et al. 2011). Optical images were acquired using ACS WFC in the  $i_{775}$  and  $z_{850}$  bandpasses in 2006 April. The total exposure times are 3320 and 16 935 s, respectively. NIR imaging in  $J_s$ - and  $K_s$  band were taken using HAWK-I in 2009 September and October with a PSF width of 0.54 and 0.43 arcsec, respectively. 52 cluster members were spectroscopically confirmed by (Hilton et al. 2010).

## APPENDIX B: CATALOGUE

**Table B1.** First lines of the catalogue of red sequence ETGs in the nine clusters considered in this work. The full table is available online.

ID	RA	Dec.	Cluster	$\log(M/M_{\odot})$	err	$R_e$ (kpc)	err	$n$	err	$bla$	err	$P(\text{ETG})$
996	28.1795	-14.0001	RXJ0152	10.50	0.07	3.10	0.31	2.90	0.06	0.77	0.011	0.80
1067	28.1716	-13.9988	RXJ0152	10.54	0.05	1.28	0.13	3.17	0.08	0.45	0.006	0.68
1340	28.2016	-13.9891	RXJ0152	10.82	0.04	2.23	0.22	4.95	0.10	0.62	0.007	0.88
1348	28.1611	-13.9889	RXJ0152	10.66	0.03	1.95	0.20	3.27	0.08	0.63	0.009	0.74
1362	28.1664	-13.9885	RXJ0152	10.63	0.11	2.25	0.23	1.50	0.05	0.99	0.019	0.86
1524	28.1653	-13.9822	RXJ0152	10.90	0.06	3.50	0.35	6.11	0.10	0.78	0.006	0.94
1559	28.1584	-13.9818	RXJ0152	10.84	0.04	1.56	0.16	5.45	0.10	0.76	0.006	0.88
1688	28.1438	-13.9782	RXJ0152	10.79	0.04	4.22	0.42	5.29	0.13	0.48	0.006	0.60
1713	28.2066	-13.9774	RXJ0152	10.68	0.05	5.54	0.55	7.10	0.21	0.72	0.009	0.86
1751	28.1704	-13.9757	RXJ0152	10.64	0.05	2.66	0.27	4.67	0.19	0.60	0.013	0.86
1763	28.2062	-13.9753	RXJ0152	11.15	0.03	2.71	0.27	4.50	0.05	0.50	0.003	0.72
1771	28.1621	-13.9754	RXJ0152	10.89	0.03	1.77	0.18	2.92	0.04	0.70	0.005	0.83
1825	28.1534	-13.9742	RXJ0152	10.74	0.13	2.33	0.23	4.90	0.10	0.64	0.007	0.93
1856	28.1797	-13.9728	RXJ0152	11.04	0.04	2.60	0.26	3.08	0.04	0.80	0.006	0.84
1900	28.1631	-13.9721	RXJ0152	10.57	0.05	1.46	0.15	4.04	0.10	0.92	0.010	0.64
1927	28.2166	-13.9708	RXJ0152	11.23	0.03	3.31	0.33	2.13	0.03	0.50	0.004	0.58
2108	28.1743	-13.9660	RXJ0152	10.96	0.03	1.74	0.17	2.26	0.03	0.72	0.005	0.65
2130	28.1787	-13.9652	RXJ0152	10.86	0.03	2.65	0.26	3.34	0.04	0.67	0.004	0.91
2167	28.1766	-13.9639	RXJ0152	11.05	0.04	3.29	0.33	4.88	0.07	0.68	0.005	0.91
2171	28.1509	-13.9634	RXJ0152	10.88	0.03	5.26	0.53	6.40	0.11	0.49	0.004	0.66
2204	28.1839	-13.9629	RXJ0152	10.61	0.04	1.85	0.18	3.10	0.06	0.80	0.008	0.93
2312	28.1791	-13.9595	RXJ0152	11.30	0.03	7.08	0.71	5.84	0.05	0.69	0.002	0.92
2385	28.1829	-13.9555	RXJ0152	11.29	0.04	5.65	0.57	5.17	0.04	0.94	0.005	0.76
2399	28.2123	-13.9584	RXJ0152	10.60	0.03	1.28	0.13	3.13	0.07	0.39	0.005	0.68

## SUPPORTING INFORMATION

Additional Supporting Information may be found in the online version of this article:

**Table B1.** First lines of the catalogue of red sequence ETGs in the nine clusters considered in this work (<http://mnras.oxfordjournals.org/lookup/suppl/doi:10.1093/mnras/stu496/-/DC1>).

Please note: Oxford University Press is not responsible for the content or functionality of any supporting materials supplied by the authors. Any queries (other than missing material) should be directed to the corresponding author for the article.

This paper has been typeset from a  $\text{\TeX}/\text{\LaTeX}$  file prepared by the author.